UNIVERSITY
OF TRENTO

DEPARTMENT OF INFORMATION AND COMMUNICATION TECHNOLOGY

38050 Povo – Trento (Italy), Via Sommarive 14
http://www.dit.unitn.it

ANALYSIS OF THE STABILITY AND ROBUSTNESS OF THE ITERATIVE MULTI-SCALING APPROACH FOR MICROWAVE IMAGING APPLICATIONS

Salvatore Caorsi, Massimo Donelli, and Andrea Massa

August 2004

Technical Report DIT-04-074

Analysis of the Stability and Robustness of the Iterative Multi-Scaling Approach for Microwave Imaging Applications

Salvatore Caorsi*, Massimo Donelli**, and Andrea Massa**

*Department of Electronics

University of Pavia, Via Ferrata 1, 27100 Pavia - Italy

Tel. +39 0382 505661, Fax +39 0382 422583

**Department of Information and Communication Technology

University of Trento, Via Sommarive 14, 38050 Trento - Italy

Tel. +39 0461 882057, Fax +39 0461 882093,

E-mail: *andrea.massa@ing.unitn.it, massimo.donelli@dit.unitn.it*

Analysis of the Stability and Robustness of the Iterative Multi-Scaling Approach for Microwave Imaging Applications

Salvatore Caorsi*, Massimo Donelli**, and Andrea Massa**

Abstract

In a reconstruction procedure based on the iterative solution of inverse scattering integral equations, the quality of the final image depends on both the numerical and experimental noise. Numerical noise is related to the accuracy of the numerical representation of the microwave imaging apparatus and system geometry. Experimental noise refers to the non-ideal electromagnetic conditions in which the data acquisition is performed. This paper provides a systematic evaluation of the impact of the most significant sources of numerical and experimental noise on the reconstruction quality when the Iterative Multi-Scaling Approach (IMSA) is used. The assessment of the robustness and stability of the IMSA is carried out by considering synthetic as well as real data. The achieved results provide detailed indications on the range of applicability of the IMSA for qualitative and/or quantitative imaging purposes.

Keywords:

Microwave Imaging, Inverse Scattering, Iterative Multi-scaling Method, Numerical Assessment.

Index Terms:

6982 Radio Science: Tomography and imaging; 0629 Electromagnetics: Inverse scattering; 0669 Electromagnetics: Scattering and diffraction; Electromagnetics: Numerical methods.

1 Introduction

Applications of imaging and detection by using scattered field data range from far-field imaging [*Franceschetti and Lanari*, 1999] to near field-imaging by considering microwave [*Bolomey*, 1991, 1995; *Zoughi*, 2000] as well as other electromagnetic frequencies [*Kak and Slaney*, 1988; *Baltes*, 1980]. Many of these imaging applications can be dealt within the same methodological framework. Then, it turns out to be very attractive and justified to study numerical approaches able to solve fundamental problems of inverse scattering since any scientific advance in a particular application automatically (or in an indirect way) provides a useful contribution for the progress in related fields.

A brief review of the more recent literature shows that a large number of very effective iterative nonlinear procedures has been proposed. Starting from an initial guess, the parameters of interest are iteratively updated by minimizing a suitably defined cost function involving the measured scattered field data. Generally speaking, two methodological approaches can be highlighted depending on whether the field inside the investigation domain is computed as a solution of the direct problem (in correspondence with the best estimate of the dielectric distribution) at each iteration [*Joachimowicz et al.*, 1991; *Chew and Wuang*, 1990; *Franchois and Pichot*, 1997] or as another unknown to be determined during the minimization procedure [*Kleinman and Van den Berg*, 1992; *Van den Berg and Abubakar*, 2001]. The IMSA [*Caorsi et al.*, 2003] belongs to the second class of iterative procedures. It is devoted to fully exploit all the available information content of scattered data. Due to the limited amount of information content in the input data, it would be problematic to parameterize the investigation domain in terms of a large number of pixel values (in order to achieve a satisfying resolution level in the reconstructed image). In order to overcome this drawback, an iterative parameterization of the test domain, performing a synthetic zoom on the region to whom the scatterer belongs, allows to achieve the required reconstruction accuracy only in the "significant" region under test.

Such a technique has yielded very promising results in processing preliminary syn-

thetic test cases [*Caorsi et al.*, 2003]. However, in order to develop a reliable reconstruction method robust to both modeling errors and uncertainties on data, it is mandatory to evaluate its limitations through accurate investigations. Consequently, a better understanding of the operational capabilities of the IMSA requires an extended assessment of the noise robustness as well as a systematic study of the impact of both experimental and model errors. Towards this end, this paper is aimed at providing an assessment of the effects of the major sources of experimental and model noise on the quality of the reconstruction. Accordingly, synthetic as well as laboratory-controlled experiments are taken into account in order to evaluate the effectiveness of the approach in dealing with customized scenarios as well as reference benchmarks.

The paper is organized as follows. Firstly, an outline of the iterative multi-scaling approach will be concisely described (Sec. 2). Sections 3 and 4 will present selected representative results for illustrating the effects of the most critical experimental and numerical parameters on the reconstruction accuracy. Final comments and conclusions will be drawn in Section 5.

2 Mathematical Formulation

Let us take as a starting point the nonlinear multi-resolution inversion approach proposed in [*Caorsi et al.*, 2003], briefly recalled in the following. At each fixed frequency f, the two-dimensional inverse scattering problem can be mathematically described through the *data equation* and the *state equation* [*Jones*, 1964]

$$E^v_{scatt}(x,y) = -j\frac{k_0^2}{4}\int\int_{D_I} \tau(x',y')E^v_{tot}(x',y')H_0^{(2)}(k_0\rho)\,dx'dy' \quad (x,y)\in D_M \tag{1}$$

$$E^v_{inc}(x,y) = E^v_{tot}(x',y') + j\frac{k_0^2}{4}\int\int_{D_I} \tau(x',y')E^v_{tot}(x',y')H_0^{(2)}(k_0\rho)\,dx'dy' \quad (x,y)\in D_I \tag{2}$$

$v = 1,...,V$ being the index indicating different multi-illumination/multi-view positions and $\rho = \sqrt{(x-x')^2-(y-y')^2}$. Moreover, $E^v_{inc}(\,.\,)$ and $E^v_{scatt}(\,.\,)$ are the *problem data*

namely the incident electric field measured inside the *investigation domain* D_I where the unknown scattering object is supposed to be located, and the scattered electric field, collected in the *observation domain* (D_M) located outside D_I. As far as the *problem unknowns* are concerned, they are the *contrast function* $\tau(x,y)$, $(x,y) \in D_I$ describing the dielectric properties of the scenario under test and the electric field inside the investigation domain, $E^v_{tot}(x,y)$, $v = 1,...,V$, $(x,y) \in D_I$.

To retrieve the unknown functions, the IMSA performs a synthetic zoom to fully exploit the limited information content of inverse scattering data [*Bucci and Franceschetti*, 1989] allowing an accurate resolution of the scatterer under test. More in detail, the method starts ($s = 1$, s being the index related to the scaling step) from a coarse ($R = 1$, R being the index of the resolution level) representation of the investigation domain D_I and iteratively defines a sub-gridding of the area where the scatterer is located. By using the "knowledge" of the scenario under test achieved at the previous steps, the iterative approach defines an estimate of the scatterer location and occupation. This enables an efficient re-allocation of the unknowns to the "focused" area according to a multi-resolution strategy. Consequently, an higher resolution level ($R = s$) is adopted only for the reduced investigation domain where the clustering procedure has estimated the presence of the scatterer. Mathematically, the multiscaling process is implemented by considering the following algorithmic procedure. At each step ($s = 1,..,S_{opt}$) of the iterative process, a multi-scaling multi-resolution function is defined

$$\Psi^{(s)}\left\{\tau\left(x_{n_{(r)}},y_{n_{(r)}}\right),\, E^v_{tot}\left(x_{n_{(r)}},y_{n_{(r)}}\right);\, r=1,...,R=s;\, n_{(r)}=1,...,N_{(r)};\, v=1,...,V\right\} = \frac{\sum_{v=1}^{V}\sum_{m_{(v)}=1}^{M_{(v)}}\left|E^v_{scatt}\left(x_{m_{(v)}},y_{m_{(v)}}\right)-\Im_{ext}\left\{\sum_{r=1}^{R}\sum_{n_{(r)}=1}^{N_{(r)}} w\left(x_{n_{(r)}},y_{n_{(r)}}\right)\tau\left(x_{n_{(r)}},y_{n_{(r)}}\right)E^v_{tot}\left(x_{n_{(r)}},y_{n_{(r)}}\right)\right\}\right|^2}{\sum_{v=1}^{V}\sum_{m_{(v)}=1}^{M_{(v)}}\left|E^v_{scatt}\left(x_{m_{(v)}},y_{m_{(v)}}\right)\right|^2} + \frac{\sum_{v=1}^{V}\sum_{r=1}^{R}\sum_{n_{(r)}=1}^{N_{(r)}}\left|w\left(x_{n_{(r)}},y_{n_{(r)}}\right)E^v_{inc}\left(x_{n_{(r)}},y_{n_{(r)}}\right)-\Im_{int}\left\{\sum_{q_{(r)}=1}^{N_{(r)}} w\left(x_{q_{(r)}},y_{q_{(r)}}\right)\tau\left(x_{q_{(r)}},y_{q_{(r)}}\right)E^v_{tot}\left(x_{q_{(r)}},y_{q_{(r)}}\right)\right\}\right|^2}{\sum_{v=1}^{V}\sum_{r=1}^{R}\sum_{n_{(r)}=1}^{N_{(r)}}\left|w\left(x_{n_{(r)}},y_{n_{(r)}}\right)E^v_{inc}\left(x_{n_{(r)}},y_{n_{(r)}}\right)\right|^2} \tag{3}$$

where w is the weighting function

$$w\left(x_{n_{(r)}}, y_{n_{(r)}}\right) = \begin{cases} 0 & if \quad \left(x_{n_{(r)}}, y_{n_{(r)}}\right) \notin D_{(s-1)} \\ 1 & if \quad \left(x_{n_{(r)}}, y_{n_{(r)}}\right) \in D_{(s-1)} \end{cases} \tag{4}$$

and where number of discretization domains belonging to the "focused" area ($n_{(R)} = 1, ..., N_{(R)}$) is chosen equal to the essential dimension of the scattered data [*Bucci and Franceschetti*, 1989] according to the criterion defined in [*Isernia et al.*, 2001].

After the minimization of (3), where a set of conjugate-gradient iterations (k being the iteration index) is performed not modifying the discretization grid, a new focused investigation domain, $D_{(s-1)}$ is defined. Such a squared area is centered at

$$x_{c_{(s-1)}} = \frac{x_{re_{(s-1)}} + x_{im_{(s-1)}}}{2}, \quad y_{c_{(s-1)}} = \frac{y_{re_{(s-1)}} + y_{im_{(s-1)}}}{2} \tag{5}$$

$$x_{\Re(s-1)} = \frac{\sum_{r=1}^{R} \sum_{n_{(r)}=1}^{N_{(r)}} \left\{ x_{n_{(r)}} \Re\left[\tau\left(x_{n_{(r)}}, y_{n_{(r)}}\right)\right]\right\}}{\sum_{n_{(r)}=1}^{N_{(r)}} \left\{ \Re\left[\tau\left(x_{n_{(r)}}, y_{n_{(r)}}\right)\right]\right\}}, \quad R = s - 1 \tag{6}$$

$$y_{\Re(s-1)} = \frac{\sum_{r=1}^{R} \sum_{n_{(r)}=1}^{N_{(r)}} \left\{ y_{n_{(r)}} \Re\left[\tau\left(x_{n_{(r)}}, y_{n_{(r)}}\right)\right]\right\}}{\sum_{n_{(r)}=1}^{N_{(r)}} \left\{ \Re\left[\tau\left(x_{n_{(r)}}, y_{n_{(r)}}\right)\right]\right\}} \tag{7}$$

and $L_{(s-1)}$ -sided

$$L_{(s-1)} = \frac{L_{re_{(s-1)}} + L_{im_{(s-1)}}}{2} \tag{8}$$

$$L_{\Re(s-1)} = 2 \frac{\sum_{r=1}^{R} \sum_{n_{(r)}=1}^{N_{(r)}} \left\{ \frac{\rho_{n_{(r)} c_{(s-1)}} \Re\left[\tau\left(x_{n_{(r)}}, y_{n_{(r)}}\right)\right]}{max_{n_{(r)}=1,..,N_{(r)}} \left\{ \Re\left[\tau\left(x_{n_{(r)}}, y_{n_{(r)}}\right)\right]\right\}} \right\}}{\sum_{r=1}^{R} \sum_{n_{(r)}=1}^{N_{(r)}} \left\{ \frac{\Re\left[\tau\left(x_{n_{(r)}}, y_{n_{(r)}}\right)\right]}{max_{n_{(r)}=1,..,N_{(r)}} \left\{ \Re\left[\tau\left(x_{n_{(r)}}, y_{n_{(r)}}\right)\right]\right\}} \right\}} \tag{9}$$

where $\Re$ stands for the real or the imaginary part and $\rho_{n_{(r)} c_{(s-1)}} = \sqrt{\left(x_{n_{(r)}} - x_{c_{(s-1)}}\right)^2 + \left(y_{n_{(r)}} - y_{c_{(s-1)}}\right)^2}$.

Then, a noise filtering is performed in order to eliminate some artifacts in the reconstructed

image. The new dielectric distribution turns out to be:

$$\tau'(x_{n_{(r)}}, y_{n_{(r)}}) = \begin{cases} \tau_0 & if \quad \begin{cases} \tau(x_{n_{(r)}}, y_{n_{(r)}}) < \tau_{th} \\ \left(x_{n_{(r)}}, y_{n_{(r)}}\right) \notin D_{(s-1)} \end{cases} \\ \dfrac{\sum_{j=1}^{J}\{\tau(x_j, y_j)\}}{J} & if \quad \begin{cases} \tau(x_{n_{(r)}}, y_{n_{(r)}}) \geq \tau_{th} \\ \left(x_{n_{(r)}}, y_{n_{(r)}}\right) \notin D_{(s-1)} \end{cases} \\ \tau(x_{n_{(r)}}, y_{n_{(r)}}) & elsewhere \end{cases} \tag{10}$$

where τ_{th} is a fixed threshold heuristically defined ($\tau_{th} = 0.2\, max_{n_{(r)}=1,..,N_{(r)}} \left\{\tau\left(x_{n_{(r)}}, y_{n_{(r)}}\right)\right\}$, $\left(x_{n_{(r)}}, y_{n_{(r)}}\right) \in D_{(s-1)}$) and τ_0 is the value of the contrast function for the background medium. Moreover, J is the dimension of the complete neighbourhood system of the sub-domain located at $(x_{n_{(r)}}, y_{n_{(r)}})$ and (x_j, y_j) indicates a neighbouring position.
The multi-resolution procedure is iterated until a "stationary condition" for the quantitative imaging of the scatterer under test is achieved ($s = S_{opt}$). This condition holds when

$$\eta_u^{(s)} = \left\{ \frac{\left|u_{(s+1)} - u_{(s)}\right|}{\left|u_{(s+1)}\right|} \times 100 \right\} < \eta_u \qquad u = x_c, y_c, L \tag{11}$$

where η_u, $u = x_c, y_c, L$ are fixed thresholds.

Such a procedure can be easily extended to multiple-scatterers geometries by considering a suitable clustering procedure (see [*Jain*, 1989] and the references cited therein) aimed at defining the number of scatterers belonging to the investigation domain and the regions where the synthetic zoom will be performed at each step of the iterative process.

3 Numerical Analysis

The complexity of the inverse scattering problem considerably increases if one considers a real environment in which the data are collected within a certain degree of approximation

due to unavoidable measurement errors, the uncertainty in the location of the interrogating source, and the mechanical positioning of the field receivers. In this framework, different situations can be identified:

- the measures of the incident and of the scattered fields (i.e., the inverse scattering data) are affected by the experimental noise;
- the interrogating source is not completely known (or cannot be modeled accurately) or of stochastic type;
- the experimental system (and in particular the electromagnetic sensors) is moved by means of a mechanical apparatus with some tolerances in the positioning.

The analysis of these situations (equivalent to noisy scenarios - compared to the ideal situation - perturbed by various error sources) is carried out by considering a reference test case. The scattering scenario is constituted by an off-centered squared ($L^{ref} = 0.48\,\lambda$) scatterer characterized by an object function $\tau^{ref}(x,y) = 0.5$ and located at ($x_c^{ref} = -0.24\,\lambda$, $y_c^{ref} = 0.48\,\lambda$) (Fig. $1(a)$). Nevertheless, in order to allow for more general interpretations, some variations of the reference geometry (in terms of larger/smaller dimensions and inhomogeneous characteristics) will be taken into account as well. The actual scatterer is enclosed in a square investigation domain $L_I = 2.4\,\lambda$-sided and illuminated by a set of $V = 4$ TM-polarized plane waves impinging with different incident angles $\theta_v = \frac{\pi(v-1)}{V}$, $v = 1, ..., V$. The scattered field data are collected in $M_{(v)} = 21$, $v = 1, ..., V$ equally-spaced measurement points lying on a circular observation domain $\rho_{DM} = 1.7\,\lambda$ in radius. Note that, according to [*Isernia et al.*, 2001], properties of scattered fields make it possible to acquire essentially all the information available from scattering experiments by simply choosing for each view a number of measurements $M_{(v)}$ slightly larger than $N_M = 4\pi\rho_{DM}$ and that the number of independent data, arising from $\sum_{v=1}^{V} M_{(v)}$ measurements, will be given by the minimum between $\frac{\sum_{v=1}^{V} M_{(v)}}{2}$ and $\frac{N_M^2}{2}$. Consequently, the "focused area" has been discretized in $N_{(R)} = 6$ domains.

As far as the inversion method is concerned, the parametric configuration, defined in [*Caorsi et al,* 2003] and heuristically selected, has been adopted ($\eta_{x_C} = \eta_{y_C} = 1\,\%$ and $\eta_L = 5\,\%$).

In order to quantify the impact of the equivalent-noise sources on the reconstruction accuracy of the IMSA, some error figures are defined. Namely, the *center-location error* (12) and the *occupation-area error* (13) aimed at quantitatively evaluating the effectiveness in the qualitative imaging

$$\gamma = \frac{\sqrt{\left[x_{c_{(S_{opt})}} - x_c^{ref}\right]^2 + \left[y_{c_{(S_{opt})}} - y_c^{ref}\right]^2}}{\lambda} \tag{12}$$

$$\Phi = \left\{ \frac{\left| L_{(S_{opt})} - L^{ref} \right|}{L_{(S_{opt})}} \right\} \times 100 \tag{13}$$

and the *reconstruction errors* (14) which give a measure of the quantitative imaging

$$\xi_{(i)} = \sum_{r=1}^{R} \frac{1}{N_{(r)}^{(j)}} \sum_{n_{(r)}=1}^{N_{(r)}^{(j)}} \left\{ \frac{\left[\tau^{(S_{opt})}\left(x_{n_{(r)}}, y_{n_{(r)}}\right)\right] - \left[\tau^{ref}(x_{n_{(r)}}, y_{n_{(r)}})\right]}{\left[\tau^{ref}(x_{n_{(r)}}, y_{n_{(r)}})\right]} \right\} \times 100 \qquad R = S_{opt} \tag{14}$$

where $N_{(r)}^{(j)}$ ranges over the whole investigation domain ($i \Rightarrow tot$), or over the area where the actual object is located ($i \Rightarrow int$), or over the background belonging to the investigation domain ($i \Rightarrow ext$).

3.1 Effects of the Experimental Noise

The impact of the experimental noise on the effectiveness of the IMSA has been evaluated by considering synthetically-generated data to avoid the effects of other error sources. The experimental noise has been simulated by adding to the problem data additive Gaussian

noises, η_{scatt} and η_{inc}

$$\widetilde{E}^{v}_{scatt}\left(x_{m_{(v)}}, y_{m_{(v)}}\right) = E^{v}_{scatt}\left(x_{m_{(v)}}, y_{m_{(v)}}\right) + \eta_{scatt}\left(x_{m_{(v)}}, y_{m_{(v)}}\right) \quad (x_{m(v)}, y_{m(v)}) \in D_M \tag{15}$$

$$\widetilde{E}^{v}_{inc}\left(x_n, y_n\right) = E^{v}_{inc}\left(x_n, y_n\right) + \eta_{inc}\left(x_n, y_n\right) \quad (x_n, y_n) \in D_I \tag{16}$$

with zero mean value and standard deviations given by

$$dev\left\{\eta_{scatt}\right\} = \frac{\sum_{v=1}^{V}\sum_{m_{(v)}=1}^{M_{(v)}}\left|E^{v}_{scatt}\left(x_{m_{(v)}}, y_{m_{(v)}}\right)\right|^2}{2\left\{\sum_{\nu=1}^{V} M_{(v)}\right\}(SNR)_{scatt}} \tag{17}$$

and

$$dev\left\{\eta_{inc}\right\} = \frac{\sum_{v=1}^{V}\sum_{r=1}^{R}\sum_{n_{(r)}=1}^{N_{(r)}}\left|E^{v}_{inc}\left(x_{n_{(r)}}, y_{n_{(r)}}\right)\right|^2}{2\left\{\sum_{r=1}^{R} N_{(r)}\right\}(SNR)_{inc}} \tag{18}$$

SNR being the signal-to-noise ratio.

For determining the effects of the noise on the reconstruction, several simulations have been performed with different values of the signal-to-noise ratio ranging between 5 and $100\,dB$. Since the non-deterministic nature of the gaussian noise, ten independent realizations of the noise process with the same SNR have been performed. For a set of selected SNR values, the tomographic images have been reconstructed and samples of the reconstructions compared with the image of the noiseless case ($(SNR)_{inc} = (SNR)_{scatt} = \infty$ - Fig. 1.(b), where the dashed lines indicate the region occupied by the actual structure). As expected, the quality of the reconstructed image is a decreasing function of the SNR. Such a behavior is also confirmed by the values of the error figures (Tab. I) and from the color-level representation of the error figures given in Fig. 2 where each sample point is the average of the results of repeated realizations. However, the IMSA demonstrates its effectiveness showing a good accuracy in the estimate of the location ($\gamma \leq 5.50 \times 10^{-2}$ and $Av\left\{\gamma\right\} = 1.13 \times 10^{-2}$ with a wide region ($(SNR)_{scatt} \geq 20\,dB$, $(SNR)_{inc} \geq 20\,dB$) in which $\gamma \cong 5.0 \times 10^{-3}$ (Fig. 2(a))) as well as of the shape of the unknown scatterer

($Av\{\Phi\} = 4.40$ %). Acceptable errors in the quantitative imaging of the investigation domain ($Av\{\xi_{tot}\} = 0.72$ % and $Av\{\xi_{ext}\} = 0.48$ %) are obtained as well. On the other hand, it should be pointed out that there are not significant differences on the reconstruction if the additive gaussian noise is added to the scattered data or to the incident field.

In order to further assess the effectiveness of the IMSA in dealing with the experimental noise of Gaussian type, going from the reference geometry to more general scenarios, different positions (Fig. 3), various dimensions of the square object (Fig. 4), and some variations in the conductivity (Fig. 5) of the scatterer under test when $(SNR)_{scatt} = (SNR)_{inc} = 20\,dB$ have been analyzed.

Concerning the dependence of the reconstruction on the scatterer position ($\frac{d}{\lambda}$ being the distance of the scatterer center from the reference-system origin), the achieved results confirm the effectiveness of the IMSA in terms of localization (Fig. $3(a)$) as well as accuracy in the reconstruction of the dielectric profile (Fig. $3(b)$). As expected, the error parameters slightly increase for the off-centered targets, but their values ($\gamma \leq 1.60 \times 10^{-2}$, $\Phi \leq 16.00$ %, $\xi_{(tot)} \leq 1.2$ %) seem to be acceptable in the range $0 < d < 1.107\,\lambda$ and allow accurate reconstructions.

Similar conclusions can be carried out from the analysis of the sensibility of the method to the object dimensions. More in detail, it should be observed that the accuracy improves in correspondence with an increment of the area of the object (Fig. 4). However, non-so-significant differences turns out to be in the qualitative ($11.0 \leq \Phi \leq 13.40$ % - Fig. $4(a)$) as well as in the quantitative imaging of the scenario under test ($\xi_{(tot)} \cong 1.0$ % - Fig. $4(b)$). On the contrary, the performances of the approach reduces when the conductivity of the scatterer increases (Fig. 5). In particular, the object area is overestimated ($\Phi|_{\sigma=1.0} \cong 13.40$ %) and the value of the reconstruction error is greater than $\xi_{(tot)} \geq 5$ % when $\sigma \geq 0.5\,S/m$.

Since the experimental error represents one of the main problem in dealing with real inverse scattering problem, for completeness the effects of a systematic (but non-Gaussian)

additive noise are analyzed as well. Towards this aim, a random white noise has been added to the data samples according to the following procedure

$$\widetilde{E}^{v}_{scatt}\left(x_{m_{(v)}}, y_{m_{(v)}}\right) = E^{v}_{scatt}\left(x_{m_{(v)}}, y_{m_{(v)}}\right) + \alpha_{scatt} E^{v}_{scatt}\left(x_{m_{(v)}}, y_{m_{(v)}}\right) \quad (x_{m(v)}, y_{m(v)}) \in D_M \tag{19}$$

$$\widetilde{E}^{v}_{inc}\left(x_n, y_n\right) = E^{v}_{inc}\left(x_n, y_n\right) + \alpha_{inc} E^{v}_{inc}\left(x_n, y_n\right) \quad (x_n, y_n) \in D_I \tag{20}$$

where α_{scatt} and α_{inc} are two random numbers varying from -1 to 1.

The inversion results when the synthetic data are corrupted by increasing the amount of random additive white noise are presented. As representative parameters, the localization error and the total reconstruction error are shown in Figs. $6(a)$ and $6(b)$, respectively. The IMSA is able to correctly localize the reference scatterer with an error γ ranging from 1.27×10^{-2} to 7.50×10^{-1}. Moreover, the reconstruction error $\xi_{(tot)}$ turns out to be lower than 10 % in a large set of values ($0.0 \leq \alpha_{scatt} \leq 0.6$, $0.0 \leq \alpha_{inc} \leq 0.7$). It seems to assess the good ability of the method in suppressing the data-noise.

3.2 Effects of the Numerical Noise

Receiver Positioning

During the inversion procedure, the knowledge of the inverse scattering data is required as well as the coordinates where these measurements are collected. However, because of the tolerance of the mechanical positioning apparatus, some differences occur between the actual positions of the measurement points and those simulated in the numerical procedure. Numerically, such a situation is equivalent to a numerical noise corrupting scattering data. In order to avoid incorrect reconstructions, it should be taken into account. From a

numerical point-of-view, it is convenient to simulate this scenario by considering, instead of the original measurement points $(x_p, y_p) \in D_P$, $p = 1, ..., P$, (where p can range over the investigation domain ($p \Rightarrow n$, $D_P \Rightarrow D_I$) or over the observation domain ($p \Rightarrow m(v)$, $D_P \Rightarrow D_M$)), alternative (or *noisy*) observation points $(\widetilde{x}_p, \widetilde{y}_p)$ whose positions are randomly chosen so that the following condition be fulfilled

$$(\widetilde{x}_p, \widetilde{y}_p) \in C_\Delta(x_p, y_p) \tag{21}$$

where $C_\Delta(x_p, y_p)$ is a circle, $\Delta = t \cdot \frac{min_p\{\rho_{p,\,p-1}, \rho_{p,\,p+1}\}}{2}$ in radius ($t \in (0, 1)$ being a random number and $\rho_{i,\,j} = \sqrt{(x_i - x_j)^2 + (y_i - y_j)^2}$), centered at the p-*th* measurement point. More in detail, Δ approximates the maximum error of the measurement system. It is related to the accuracy of the experimental positioning apparatus (which strongly depends on the application, but generally it is lower than few millimeters [*Franchois et al.*, 1998]). Then, measured data collected at $(\widetilde{x}_p, \widetilde{y}_p)$ are assumed as input data at (x_p, y_p).

Figure 7 shows the values of the averaged error figures for different values of the positioning parameters $(t)_{inc}, (t)_{scatt} \in [0, 1]$. The pictures show that the reconstruction capabilities strongly depends on the positioning of the scattered-field sensors. As far as the localization error is concerned, it turns out to be that $8.03 \times 10^{-3} \leq \gamma \leq 6.78 \times 10^{-1}$ and on average its value is equal to $Av\{\gamma\} = 1.88 \times 10^{-1}$ (greater of about one order in magnitude as compared with the average value related to the experimental noise, 1.88×10^{-1} vs. 1.13×10^{-2}) with a large variance ($Var\{\gamma\} = 2.36 \times 10^{-2}$). Larger errors occur when $(t)_{scatt} \geq 0.65$ and a wrong location of the scatterer in the region defined by ($(t)_{scatt} \geq 0.85$, $(t)_{inc} \geq 0.30$). On the other hand, Φ (Fig. 7(b)), ξ_{tot} (Fig. 7(c)), and ξ_{ext} (Fig. 7(e)) present a step-like behavior (with the amplitude of the errors almost independent of $(t)_{inc}$) confirming the strong impact of $(t)_{scatt}$ on the retrieval process. More in detail, it happens that 0.17 %$\leq \Phi \leq$14 %, 0.27 % $\leq \xi_{tot} \leq$3 %, and 1.34×10^{-3}%$\leq \xi_{ext} \leq$ 0.9 % for $(t)_{scatt} \leq 0.65$ with a nonnegligible increase otherwise.

For completeness, Figure 8 shows some examples of the reconstructions for different tol-

erances of the mechanical positioning system. As previously indicated, the reconstruction accuracy decreases in a more significant way with the increase of $(t)_{scatt}$ (Figs. 8(a)-(c)) if compared to the corresponding increase in $(t)_{inc}$ (Figs. 8(d)-(f)) as confirmed from the values of the error figures reported in Tab. II. As an example, let us consider the images related to ($(t)_{scatt} = 1.0$, $(t)_{inc} = 0.0$) (Fig. 8(c)) and to ($(t)_{scatt} = 0.0$, $(t)_{inc} = 1.0$) (Fig. 8(f)). Fig. 8(f) shows that even though the shape and the geometric informations are not accurately estimated ($\Phi = 25.24$ % and $\xi_{int} = 12.97$ %), a structure can be identified in roughly the correct location ($\gamma = 1.58 \times 10^{-2}$, $\xi_{tot} = 2.09$ % and $\xi_{ext} = 1.42$ %). On the contrary, a collection of small squares exist in a region close the actual object and multiple artifacts are present in the background. This produces a poor reconstruction ($\gamma|_{(t)_{scatt}=1.0,(t)_{inc}=0.0} \cong 17 \times \gamma|_{(t)_{scatt}=0.0,(t)_{inc}=1.0}$, $\xi_{tot}|_{(t)_{scatt}=1.0,(t)_{inc}=0.0} \cong 4.5 \times \xi_{tot}|_{(t)_{scatt}=0.0,(t)_{inc}=1.0}$ and $\xi_{ext}|_{(t)_{scatt}=1.0,(t)_{inc}=0.0} \cong 6 \times \xi_{ext}|_{(t)_{scatt}=0.0,(t)_{inc}=1.0}$) (Fig. 8($c$)).

To give an idea of the connection between tolerances and positions of the receivers as well as amplitudes of inverse scattering data, Figs. 9 and 10 show the plots of the locations of the field sensors (a) and related measured data for different values of $(t)_{scatt}$ and $(t)_{inc}$, respectively.

In order to generalize previous indications and according to the assessment strategy used in Subsection 3.1, several numerical experiments have been carried out by assuming a noisy scenario characterized by $(t)_{scatt} = 0.1$ and $(t)_{inc} = 0.2$. Figure 11 summarizes the obtained results in terms of reconstruction errors. As can be observed, the total reconstruction error ξ_{tot} is almost constant both for different positions (0.5 % $\leq \xi_{tot} \leq$0.6 %) and for different dimensions (4.1 % $\leq \xi_{tot} \leq$5 %) of the reference scatterer. On the contrary, larger differences turn out to be by increasing the scatterer conductivity with an increment of the error values of about one order in magnitude (1.0 % $\leq \xi_{tot} \leq$12.5 % and 0.9 % $\leq \xi_{ext} \leq$10.1 %).

Interrogating Source Location

To evaluate the effects of a non-completely known or stochastic source on the incident electric field and consequently on the reconstruction algorithm (which assumes the incident field radiated by a deterministic source), let assume that the plane wave radiated by the electromagnetic source instead of propagating in the direction

$$\overrightarrow{k_\nu} = k_0 \left\{ cos\left(\theta_\nu\right) \overrightarrow{x} + sin\left(\theta_\nu\right) \overrightarrow{y} \right\} \tag{22}$$

propagates in another direction

$$\overrightarrow{\widetilde{k}_\nu} = k_0 \left\{ cos\left(\theta_\nu + \widetilde{\theta}_\nu\right) \overrightarrow{x} + sin\left(\theta_\nu + \widetilde{\theta}_\nu\right) \overrightarrow{y} \right\} \tag{23}$$

where $k_0 = 2\pi f \sqrt{\varepsilon_0 \mu_0}$ and $\widetilde{\theta}_\nu$ is a random variable uniformly distributed in the range $\zeta\left(-\frac{\pi}{V}, \frac{\pi}{V}\right)$ (ζ being a random number in the range $(0, 1)$)

The results of a large set of simulations (repeated ten times for each value of ζ in order to give accurate statistical informations) are presented in Fig. 12 in terms of qualitative (Fig. $12(a)$) and quantitative error figures (Fig. $12(b)$). In general, the errors increase proportionally to ζ, except for the *total reconstruction error*. In such a case, a knee is present for a threshold value equal to $\zeta_{th} \cong 0.4$, which separates two saturation regions ($\xi_{ext} \cong 0.7$ % for $\zeta_{th} < 0.4$ and $\xi_{ext} \cong 1.5$ % otherwise). Nevertheless, the same level of performances as was seen in the examples related to the experimental noise (sub-Sec. 3.1) can be observed here (Tab. III). An accurate localization is achieved ($\gamma = 5.81 \times 10^{-3}$ for $\zeta = 0.25$ and $\gamma = 8.76 \times 10^{-2}$ for $\zeta = 1.0$) as pictorially resumed in Fig. 13. On the other hand, with the increment of ζ, noticeable errors in the object shaping as well as in the dielectric reconstruction occur and the scatterer cannot be exactly shaped. However, the IMSA is always (also for $\zeta = 1.0$) able to retrieve a structure that occupies a large subset of the true scatterer.

Finally, for completeness, selected results of a "generalization" study are presented in

Fig. 14. The values of the total error are presented versus ζ and for different scattering scenarios. As expected (according to the conclusions drawn in previous subsections) largest variations occur for dissipative objects (e.g., 6.0 % $\leq \xi_{tot} \leq$12.7 % when $\zeta = 1.0$ - Fig. 14(c)). As far as other test cases are concerned, ξ_{tot} ranges between 0.5 % and 4.0 % (Fig. 14(a)) and from 0.5 % up to 1.5 % (Fig. 14(b)) whatever the scatterer position and dimension, respectively.

4 Validation against Experimental Data

Through the numerical analysis carried out in Sec. 3, it has been shown that the IMSA is effective in reconstructing the contrast of penetrable objects and an accurate qualitative imaging of the scenario under test can be obtained. Moreover, the stability of the method with respect to realistic sources of electromagnetic noise has been verified. However, previous tests are concerned with synthetic (i.e. numerically simulated) scattering experiments. To fully assess the imaging capabilities of the IMSA when a realistic scenario is dealt with, some experiments with real-data have been also considered. More in detail, the validation against experimental data is motivated by:

- the need of validating the proposed approach on a benchmark and to judge its contribution in the framework of inverse scattering algorithms completing the validation performed with synthetic data (undoubtedly real-data does not allow one to evaluate the performances of a method in an exhaustive set of possible scenario as in the case of numerically generated data but state a common benchmark);

- the need of avoiding an *inverse crime* [*Colton and Kres*, 1992] consisting in testing the inversion algorithm on a data-set generated by a forward solver closely related to that used during the inversion process;

- the need of evaluating the accuracy of the approach in dealing with independent laboratory-controlled experiments. It is evident that the transfer of an inversion

procedure to industrial applications greatly depends on demonstrating them successfully with experimental data. This not only guarantees that the scattering data are fully independent to the inverse scattering algorithm, but also check the sensitivity of the algorithm to realistic noise and modeling errors;

- the need of estimating the feasibility of synthetic scenarios with respect to experimental ones in order to state the significance of numerical testing.

In order to perform the experimental validation, the multiple-frequency angular-diversity bistatic data provided by the Institut Fresnel, Marseille, France [*Belkebir et al*, 2000] represent a significant benchmark. The data are obtained in a controlled environment where the target and the electromagnetic source are known and instrumental and experimental errors jointly occur. In particular, the availability of data measured at different frequencies provides a good opportunity to evaluate various noisy conditions on the same scattering geometry. Towards this end, all the reconstructions have been computed starting from data of one single frequency, avoiding multi-frequency [*Belkebir et al*, 1997] or frequency-hopping approaches [*Ferraye et al.*, 2003] that certainly could greatly improve the retrieval accuracy.

More in detail, the experimental setup consists of a 2D bistatic measurement system with an emitter placed at a fixed position, while a receiver is rotating with an arm along the vertical cylindrical scatterer under test. The antennas are double ridged horn antennas linearly polarized with a frequency range from $1\,GHz$ to $18\,GHz$. The distances between emitter-center and receiver-center of the experimental setup are set to $720\,mm \pm 3\,mm$ and $720\,mm \pm 3\,mm$, respectively. The target rotates from 0 to 350 in steps of 10. The rotation of the receiver is from 60 to 300 in steps of 5. Obviously, the *aspect-limited* nature of the measurement setup leads to a reduction of the available information. Consequently, all $V = 36$ available views and, for each of them, $M_{(v)} = 49$, $v = 1, ..., V$, are used for the reconstruction.

The first test case is related to a single circular dielectric cylinder and the corresponding dataset "dielTM_dec8f.exp" is considered. The cylinder (characterized by an estimated object function equal to $\tau^{ref}(x,y) = 2.0 \pm 0.3$) of circular cross-section ($L^{ref} = 30\,mm$ in diameter), is located at ($x_c^{ref} = 0.0$, $y_c^{ref} = -30\,mm$) by assuming the coordinate reference system centered at the center of the experimental setup (a detailed description of the underlying experimental setup as well as of the data sets is given in [*Belkebir and Saillard*, 2001] and [*Belkebir et al.*, 2000]). Moreover, it is assumed to belong to a square investigation domain of $30 \times 30\,cm^2$. The results of the reconstructions, starting from the free-space configuration, are shown in Fig. 15. As can be observed, the reconstruction accuracy is very low in correspondence with the smallest frequency ($f = 1\,GHz$) and for the higher frequencies ($f = 7 - 8\,GHz$) where the reconstructed objects are diffused over a large part of the investigation domain (causing an overestimate of the occupation area, $L_{(S_{opt})}\Big|_{f=7\,GHz} = 97.06\,mm$ and $L_{(S_{opt})}\Big|_{f=8\,GHz} = 76.46\,mm$). On the contrary, the location and the size of the object are satisfactorily retrieved at the intermediate frequencies (implicitly, the similarity on the geometric and dielectric estimates (Tab. IV) seems to indicate stable noisy conditions of the experimental setup in such a frequency range) with a notable improvement in the resolution accuracy as confirmed in Tab. IV. The maximum value of the estimated object function slightly exceeds the expected one to compensate the unavoidable smoothing in the reconstruction and it turns out to be within the given tolerance of the reference profile. These results further confirms the effectiveness of the IMSA also in considering aspect-limited data (as for the case of "Marseille" experiments).

In order to validate the multi-scaling inversion procedure on metallic-type targets, two sets at a fixed frequency ($f = 4\,GHz$) from the database are then considered. These examples are concerned with a centered (Fig. 16(a)) - "rectTM_cent.exp") and an off-centered (Fig. 16(b) - "rectTM_dece.exp") rectangular cylinders whose dimensions are $25.4 \times 12.7\,mm^2$. Under the assumption that the scatterers are highly conducting, the real part of the contrast has been ignored. Moreover, following the indications reported in

[*Van den Berg et al*, 1995], if at some point in the iterative minimization the reconstructed $Im\{\tau\}$ is larger than Γ_{max} the contrast is replaced by Γ_{max}. In these examples, $\Gamma_{max} = 10.5$. The reconstructed profiles are shown in Figure 16 where the exact locations of the boundaries of the actual objects are indicated by the dashed lines. These results seem to indicate that the shape of metal objects can be recovered with high quality by using the iterative multi-scaling approach. However, future works will be needed to fully evaluate (by exploiting all the features of the IMSA as well) the effectiveness of such a technique in dealing with metallic objects in a large frequency range.

For completeness, the last experiment deals with the reconstruction of a multiple-dielectric-scatterers configuration. The data related to the frequency $f = 4\,GHz$ of the "twodielTM_8f.exp" collection are used. In such a case, the actual configuration is composed of two dielectric cylinders, with the same dielectric properties described in the first experimental example, located $90\,mm$ one far from the other and placed $30\,mm$ from the center of the experimental setup. The reconstructed image (Fig. 17) gives a clear location of the two cylinders without any artifacts or ghost targets. Such a result further assess the effectiveness of the IMSA in dealing with dielectric target. Moreover, it confirms the possibility to use the approach in complex scenarios and for single as well as multiple scatterers configurations.

5 Conclusions

In this paper, a systematic evaluation of the impact of the most significant sources of numerical and experimental noise on the reconstruction capabilities of the Iterative Multi-Scaling Approach has been carried out. The performances of the approach, in terms of image quality and quantitative error parameters, have been shown for different conditions, both simulated and real. Starting from these experiments it may be stated that globally the IMSA demonstrated an acceptable stability and robustness to noisy conditions (in particular, the method turns out to be more sensitive to the accurate positioning of

the receivers than to the other noise sources and to the conductivity of the scatterer under test) allowing, also in presence of large errors in the scattering data, an accurate localization of the scatterers under test. As far as the quantitative imaging is concerned, acceptable results have been achieved thanks to the synthetic zoom allowed by the iterative multi-scaling procedure. Certainly, further refinements could be achieved by adding some penalty functions to the multi-scaling multi-resolution cost function in order to fully exploit all the available *a-priori* knowledge of the solution or by considering state-of-the-art edge-preserving regularizations leading to significant enhancements in the image reconstruction.

Acknowledgements

The experimental data used herein are by courtesy of Dr. K. Belkebir and Dr. M. Saillard (Institut Fresnel, Marseille, France). The authors wish to thank E. Vico for helpful discussions on IMSA and Ing. D. Franceschini for providing some numerical results of computer simulations.

References

Baltes, H. P. (1980), *Inverse Scattering Problems in Optics*, Springer-Verlag, Berlin, Germany.

Belkebir, K., S. Bonnard, F. Sabouroux, and M. Saillard (2000), Validation of 2D inverse scattering algorithms from multi-frequency experimental data, *J. Electromagn. Waves Appl.*, *14*, 1637-1668.

Belkebir, K., R. E. Kleinman, and Ch. Pichot (1997), Microwave imaging - Location and shape reconstruction from multifrequency scattering data, *IEEE Trans. Microwave Theory Tech.*, *45*, 469-476.

Belkebir, K., and M. Saillard (2001), Introduction to the Special Section Testing inversion algorithms against experimental data, *Inverse Problems*, *17*, 1565-1571.

Bolomey, J. Ch. (1991), Recent European developments in active microwave imaging for industrial, scientific, and medical applications, *IEEE Trans. Microwave Theory Tech.*, *37*, 2109-2117.

Bolomey, J. Ch. (1995), *Frontiers in Industrial Process Tomography*, Engineering Foundation.

Bucci, O. M., and G. Franceschetti (1989), On the degrees of freedom of scattered fields, *IEEE Trans. Antennas Propagat.*, *37*, 918-926.

Caorsi, S., M. Donelli, D. Franceschini, and A. Massa (2003), A new methodology based on an iterative multi-scaling for microwave imaging, *IEEE Trans. Microwave Theory Tech.*, *51*, 1162-1173.

Chew, W. C., and Y. M. Wang (1990), Reconstruction of two-dimensional permittivity distribution using the distorted Born iterative method, *IEEE Trans. Medical Imaging*, *9*, 218-225.

Colton, D., and R. Kress (1992), *Inverse Acoustic and Electromagnetic Scattering Theory*. Springer, Berlin.

Ferraye, R., J. Y. Dauvignac, and Ch. Pichot (2003), An inverse scattering method

based on contour deformations by means of a level set method using frequency hopping technique," *IEEE Trans. Antennas Propagat.*, *51* , 1100-1113.

Franceschetti, G., and R. Lanari (1999), *Synthetic Aperture Radar Processing Technique*, CRC Press.

Franchois, A., A. Joisel, Ch. Pichot, and J. Ch. Bolomey (1998), Quantitative microwave imaging with a 2.45 GHz planar microwave camera, *IEEE Trans. Medical Imaging.*, *17*, 550-561.

Franchois, A., and C. Pichot (1997), Microwave imaging - Complex permittivity reconstruction with a Levenberg-Marquardt method, *IEEE Trans. Antennas Propagat.*, *45*, 203-215.

Isernia, T., V. Pascazio, and R. Pierri (2001), On the local minima problem in a tomographic imaging technique, *IEEE Trans. Geosci. Remote Sens.*, *39*, 1596-1607.

Jain, A. K. (1989), *Fundamentals of Digital Image Processing*. Englewood Cliffs, USA: Prentice-Hall.

Joachimowicz, N., C. Pichot, and J.-P. Hugonin (1991), Inverse scattering: an iterative numerical method for electromagnetic imaging, *IEEE Trans. Antennas Propagat.*, *39*, 1742-1753.

Jones, D. S. (1964), *The Theory of Electromagnetism*. Oxford, U.K.: Pergamon Press.

Kak, A. C., and M. Slaney (1988), *Principles of Computerized Tomographic Imaging*, IEEE, New York.

Kleinman, E. R., and P. M. van den Berg (1992), A modified gradient method for two-dimensional problems in tomography, *J. Computat. Appl. Math.*, *42*, 17-35.

Massa, A. (2002), Genetic algorithm (GA) based techniques for 2D microwave inverse scattering, in *Recent Research Developments in Microwave Theory and Techniques*, ed. M. Pastorino, Transworld Research Network Press, Trivandrum, India, 193-218.

Van den Berg, P. M., and A. Abubakar (2001), Contrast source inversion method: state of the art, *PIER*, *34*, 189-218.

Van den Berg, P. M., M. G. Coté, and R. E. Kleinman (1995), "Blind" shape

reconstruction from experimental data, *IEEE Trans. Antennas Propagat.*, *43*, 1389-1396.

Zoughi, R. (2000), *Microwave Nondestructive Testing and Evaluation*, Kluwer Academic Publishers, The Netherlands.

Figure Captions

- Figure 1. Impact of the *experimental noise* on the reconstruction accuracy - Estimated permittivity distributions of a square homogeneous dielectric cylinder ($\tau = 0.5$). (a) Reference profile. Retrieved profile at $S = S_{opt}$ for (b) Noiseless Conditions ($(SNR)_{scatt} = (SNR)_{inc} = \infty$), (c) $(SNR)_{scatt} = \infty$ and $(SNR)_{inc} = 20\,dB$, (d) $(SNR)_{scatt} = \infty$ and $(SNR)_{inc} = 5\,dB$, (e) $(SNR)_{scatt} = (SNR)_{inc} = 20\,dB$, and (f) $(SNR)_{scatt} = (SNR)_{inc} = 5\,dB$.

- Figure 2. Impact of the *experimental noise* on the reconstruction accuracy - Color-level representation of the $(a)(b)$ qualitative and (c)-(e) quantitative error figures for different values of the signal-to-noise ratio.

- Figure 3. Impact of the *experimental noise* on the reconstruction accuracy - Values of the error figures for different positions in the investigation domain of the reference scatterer ($(SNR)_{scatt} = (SNR)_{inc} = 20\,dB$).

- Figure 4. Impact of the *experimental noise* on the reconstruction accuracy - Behavior of the error figures versus the dimensions of the scatterer under test ($(SNR)_{scatt} = (SNR)_{inc} = 20\,dB$).

- Figure 5. Impact of the *experimental noise* on the reconstruction accuracy - Dependence of the error figures on the conductivity σ of the scatterer under test ($(SNR)_{scatt} = (SNR)_{inc} = 20\,dB$).

- Figure 6. Impact of the *experimental noise* (non-gaussian model) on the reconstruction accuracy - Color-level representation of the (a) center-location error γ and of the (b) total reconstruction error ξ_{tot}.

- Figure 7. Impact of the *numerical noise* on the reconstruction accuracy (Receiver Positioning) - Color-level representation of the $(a)(b)$ qualitative and (c)-(e) quantitative error figures for different values of the positioning tolerance (t).

- Figure 8. Impact of the *numerical noise* on the reconstruction accuracy (Receiver Positioning) - Estimated permittivity distributions of a square homogeneous dielectric cylinder ($\tau = 0.5$). Retrieved profile at $S = S_{opt}$ when (a) $((t)_{scatt} = 0.2,$ $(t)_{inc} = 0.0)$, (b) $((t)_{scatt} = 0.5,$ $(t)_{inc} = 0.0)$, (c) $((t)_{scatt} = 1.0,$ $(t)_{inc} = 0.0)$, (d) $((t)_{scatt} = 0.0,$ $(t)_{inc} = 0.2)$, (e) $((t)_{scatt} = 0.0,$ $(t)_{inc} = 0.5)$, (f) $((t)_{scatt} = 0.0,$ $(t)_{inc} = 1.0)$, (g) $((t)_{scatt} = (t)_{inc} = 0.2)$, and (h) $((t)_{scatt} = (t)_{inc} = 0.5)$.

- Figure 9. Impact of the *numerical noise* on the reconstruction accuracy (Receiver Positioning) - Receivers positions (a) and scattered electric field data (b)-(c) $((b)$ $Re\left\{E^v_{scatt}\left(x_{m_{(v)}}, y_{m_{(v)}}\right)\right\}$, (c) $Im\left\{E^v_{scatt}\left(x_{m_{(v)}}, y_{m_{(v)}}\right)\right\}$, $v = 1)$ for various values of $(t)_{scatt}$.

- Figure 10. Impact of the *numerical noise* on the reconstruction accuracy (Receiver Positioning) - Receivers positions inside the investigation domain (a) and incident electric field data (b)-(c) $((b)$ $Re\left\{E^v_{inc}(x_n, y_n)\right\}$, (c) $Im\left\{E^v_{inc}(x_n, y_n)\right\}$, $v = 1)$ for various values of $(t)_{inc}$.

- Figure 11. Impact of the *numerical noise* on the reconstruction accuracy (Receiver Positioning) - Values of the *reconstruction errors* $\xi_{(i)}$, $j = tot, int, ext$ (a) for different positions, (b) for different dimensions, and (c) for different values of the conductivity of the reference scatterer $((t)_{scatt} = 0.1,$ $(t)_{inc} = 0.2)$.

- Figure 12. Impact of the *numerical noise* on the reconstruction accuracy (Interrogating Source Location) - (a) Qualitative and (b) Quantitative Error Figures for different values of ζ.

- Figure 13. Impact of the *numerical noise* on the reconstruction accuracy (Interrogating Source Location) - Estimated permittivity distributions of a square homogeneous dielectric cylinder ($\tau = 0.5$). Retrieved profile at $S = S_{opt}$ when (a) $\zeta = 0.25$, (b) $\zeta = 0.50$, (c) $\zeta = 0.75$, and (d) $\zeta = 1.0$.

- Figure 14. Impact of the *numerical noise* on the reconstruction accuracy (Interrogating Source Location) - Behavior of the *total reconstruction error* $\xi_{(tot)}$ versus ζ (a) for different positions, (b) for different dimensions, and (c) for different values of the conductivity of the reference scatterer.

- Figure 15. Experimental Validation - Reconstruction of an off-centered homogeneous circular cylinder (Real dataset "Marseille" [*Belkebir and Saillard*, 2001] - "dielTM_dec8f.exp"): (a) $f = 1\,GHz$, (b) $f = 2\,GHz$, (c) $f = 3\,GHz$, (d) $f = 4\,GHz$, (e) $f = 5\,GHz$, (f) $f = 6\,GHz$, (g) $f = 7\,GHz$, and (h) $f = 8\,GHz$.

- Figure 16. Experimental Validation (Real dataset "Marseille" [*Belkebir and Saillard*, 2001]) - Reconstruction of metallic cylinders at the frequency $f = 4\,GHz$: (a) Data set "rectTM_cent.exp" and (b) Data set "rectTM_dece.exp".

- Figure 17. Experimental Validation - Reconstruction of multiple dielectric cylinders at the frequency $f = 4\,GHz$ (Real dataset "Marseille" [*Belkebir and Saillard*, 2001] - "twodielTM_8f.exp").

Table Captions

- Table I. Impact of the *experimental noise* on the reconstruction accuracy - Error Figures.
- Table II. Impact of the *numerical noise* on the reconstruction accuracy (Receiver Positioning) - Error Figures.
- Table III. Impact of the *numerical noise* on the reconstruction accuracy (Interrogating Source Location) - Error figures Statistics.
- Table IV. Experimental Validation - Estimated geometric and dielectric parameters (f $[GHz]$; $x_{c_{(S_{opt})}}$, $y_{c_{(S_{opt})}}$, $L_{(S_{opt})}$ $[mm]$).

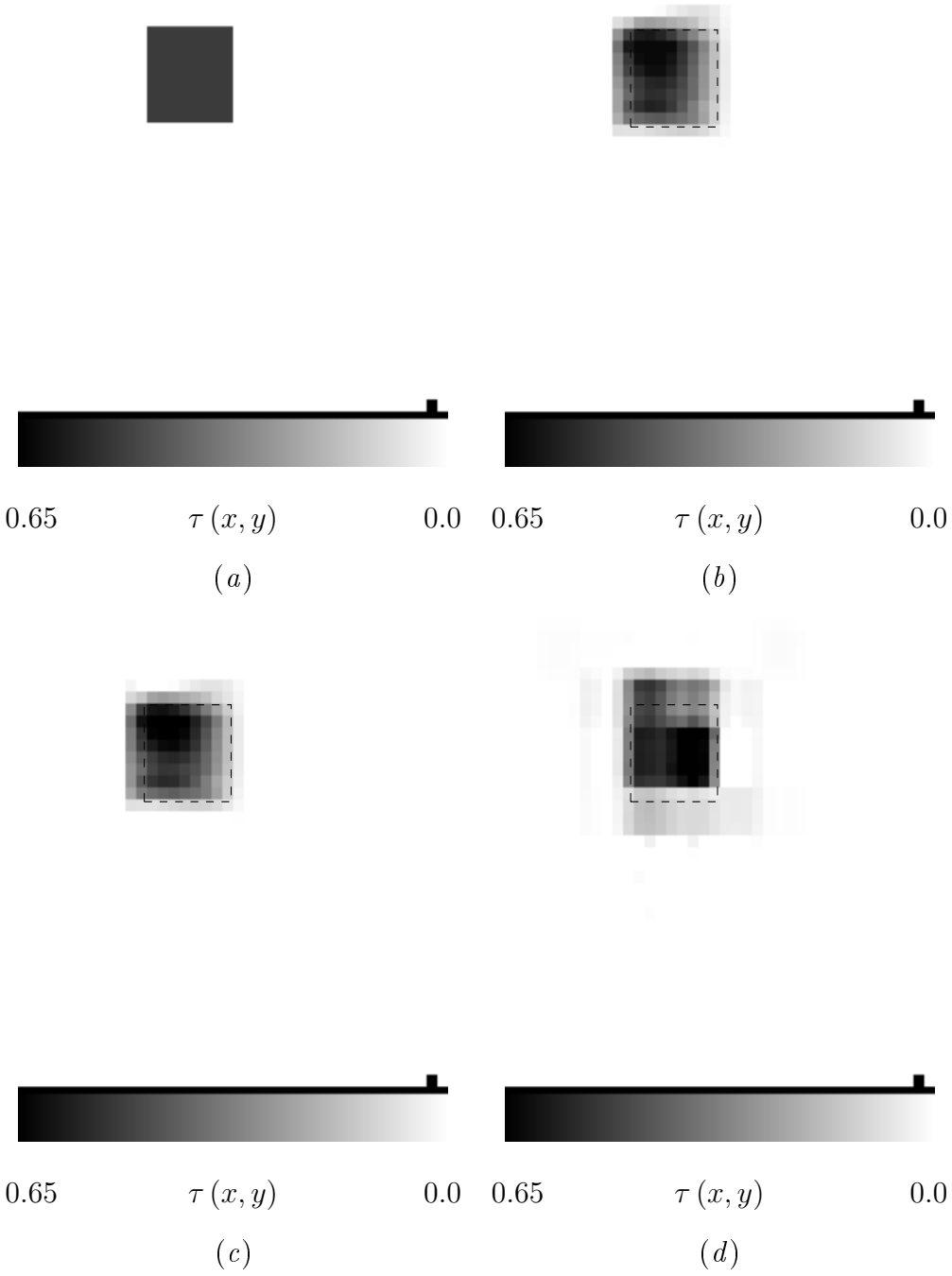

Fig. 1 (*I*) - S. Caorsi *et al.*, "Analysis of the stability ..."

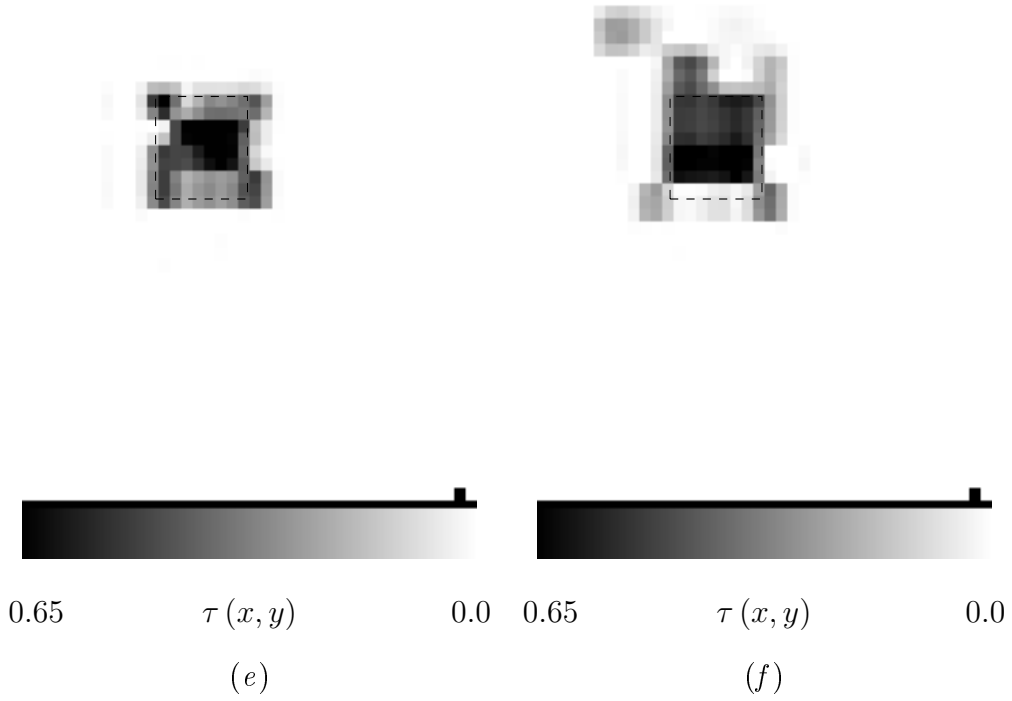

Fig. 1 (*II*) - S. Caorsi *et al.*, "Analysis of the stability ..."

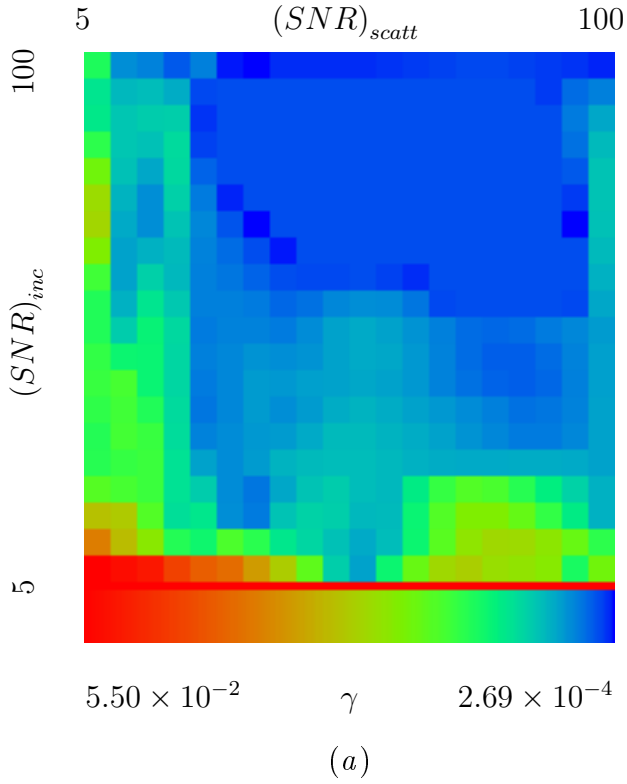

(a)

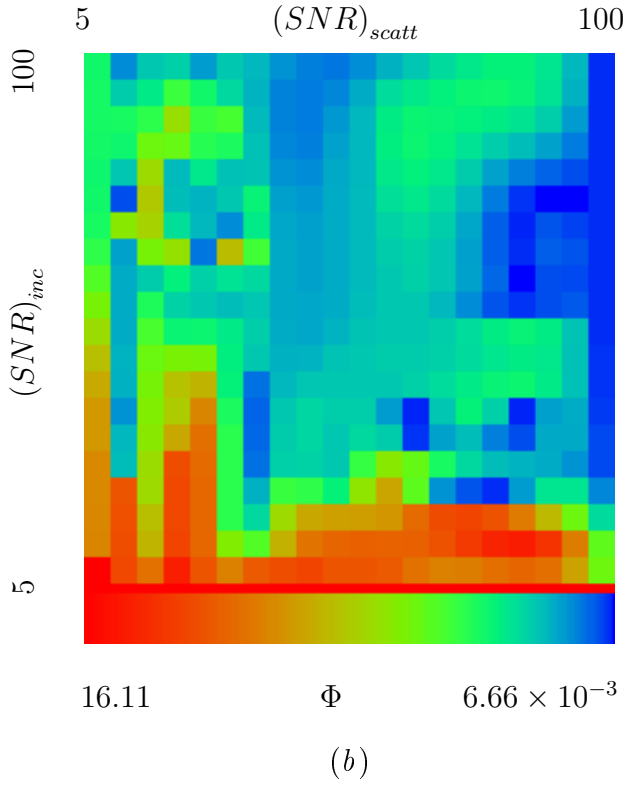

(b)

Fig. 2 (*I*) - S. Caorsi *et al.*, "Analysis of the stability ..."

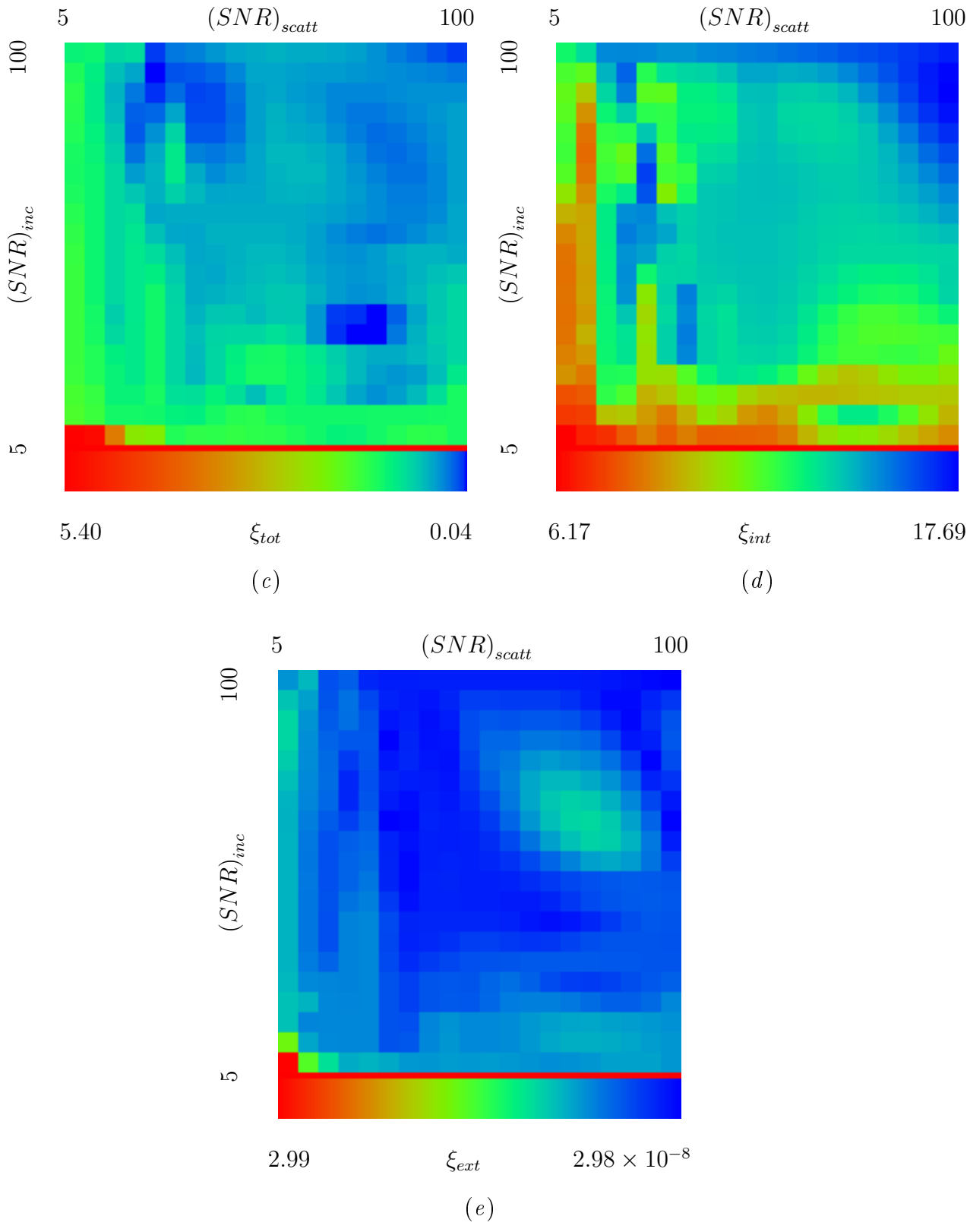

Fig. 2 (*II*) - S. Caorsi *et al.*, "Analysis of the stability ..."

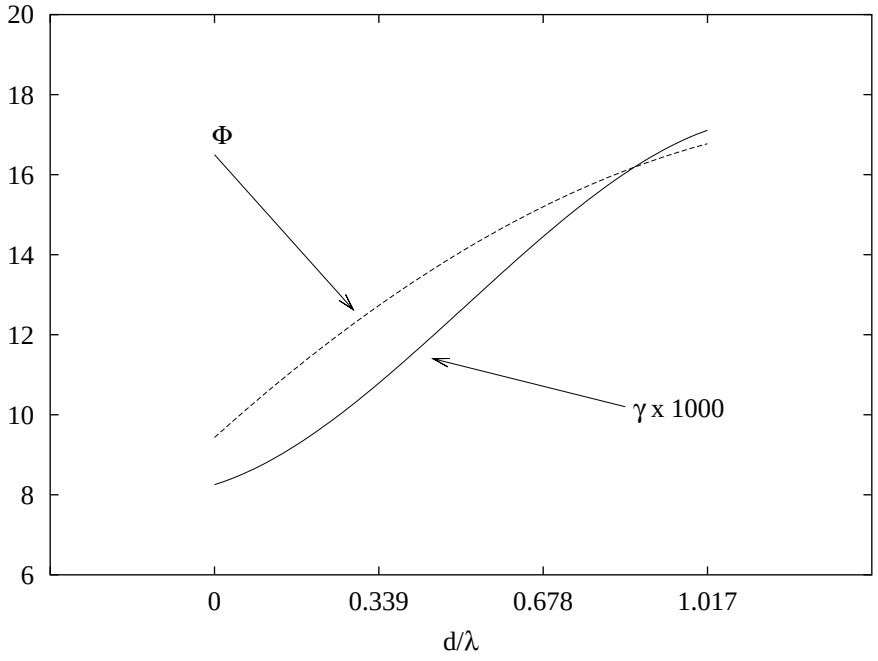

(a)

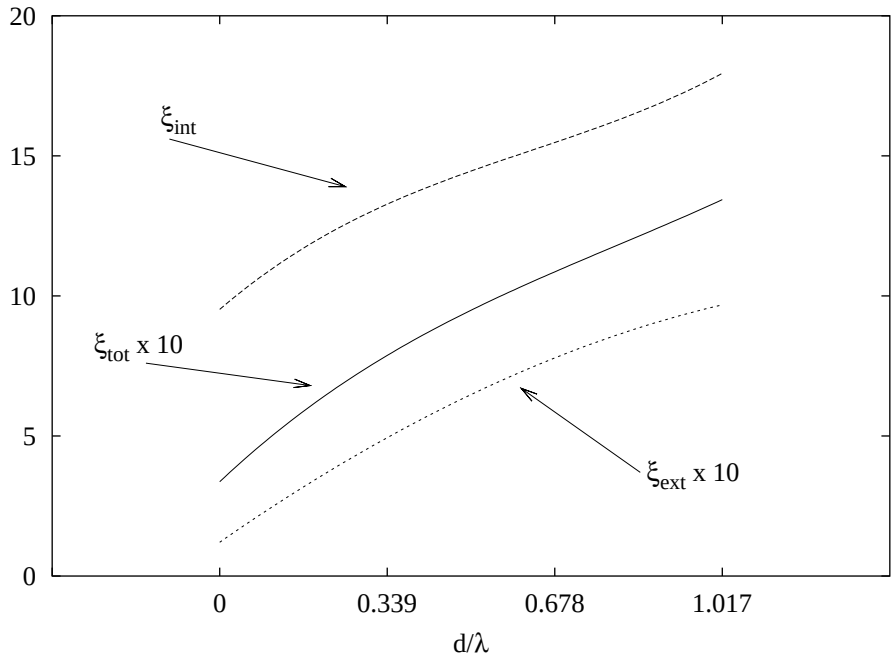

(b)

Fig. 3 - S. Caorsi *et al.*, "Analysis of the stability ..."

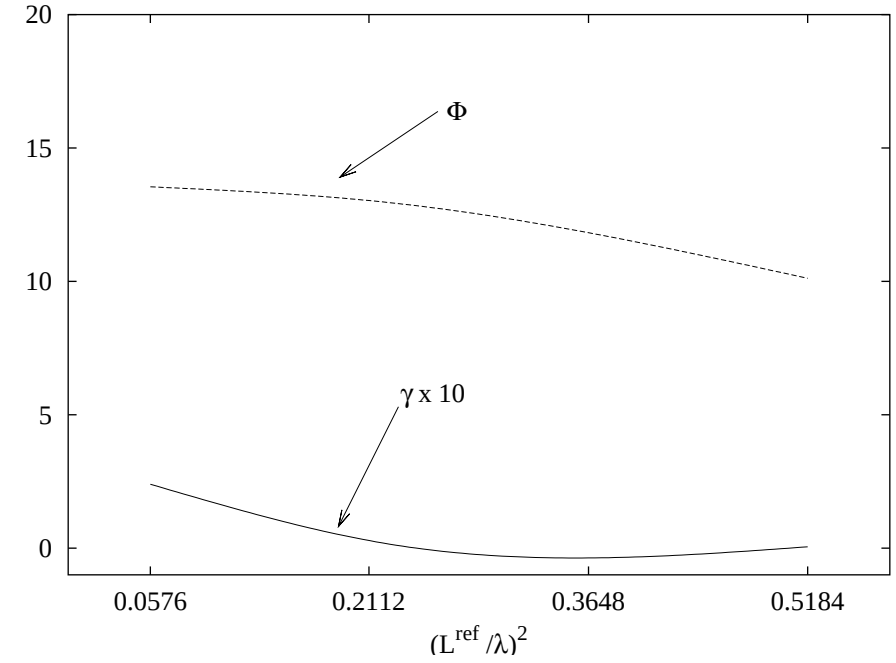

(a)

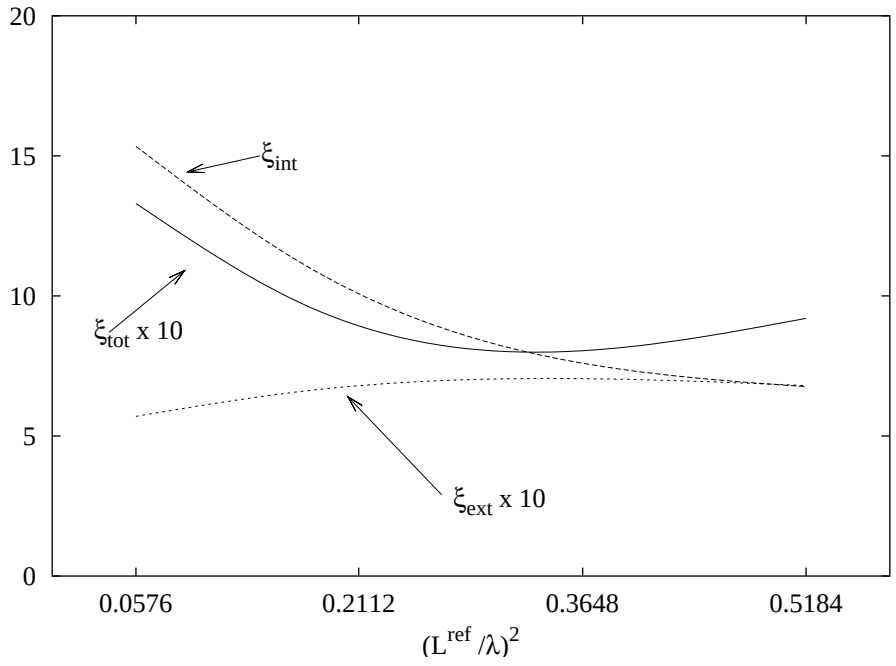

(b)

Fig. 4 - S. Caorsi *et al.*, "Analysis of the stability ..."

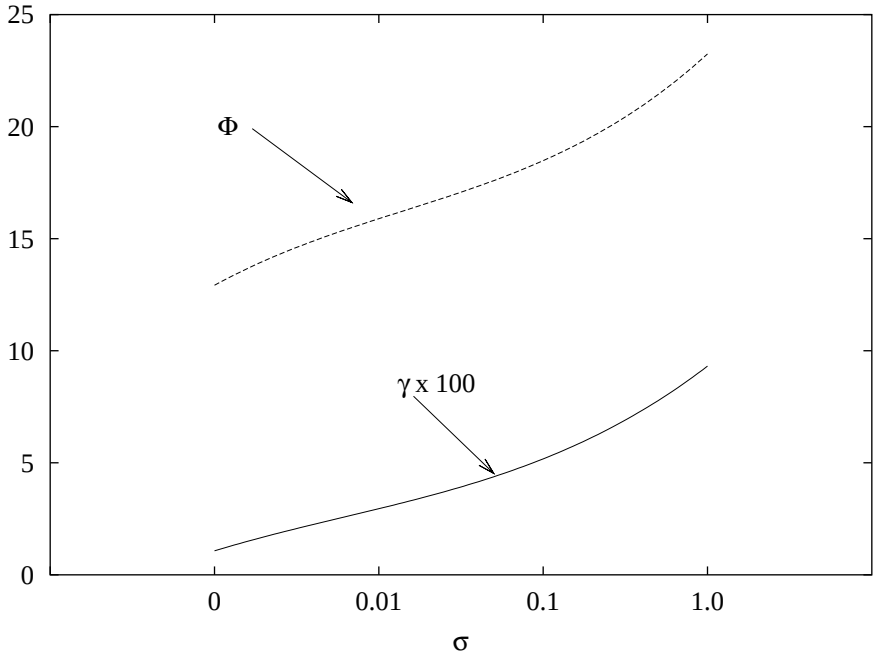

(a)

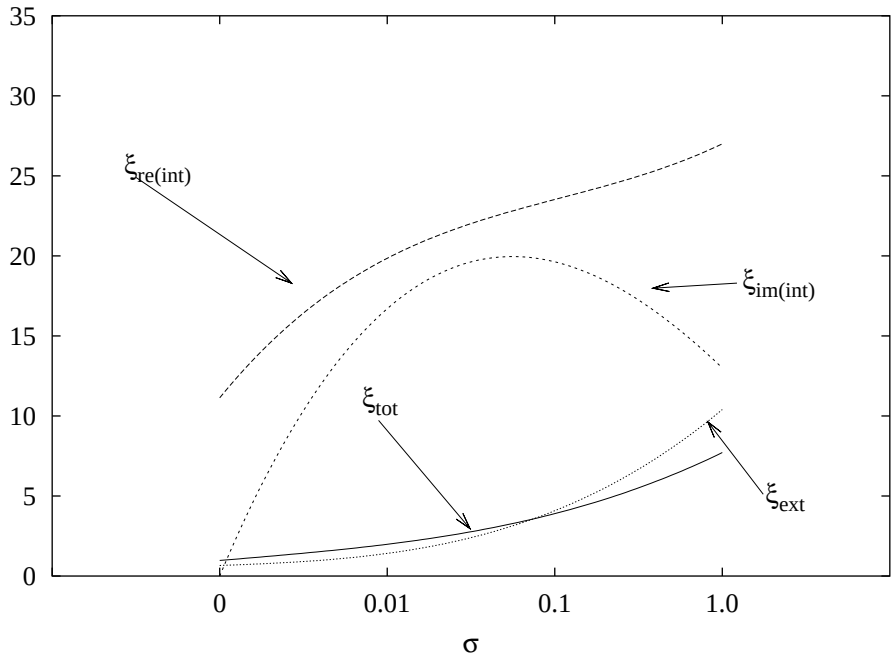

(b)

Fig. 5 - S. Caorsi *et al.*, "Analysis of the stability ..."

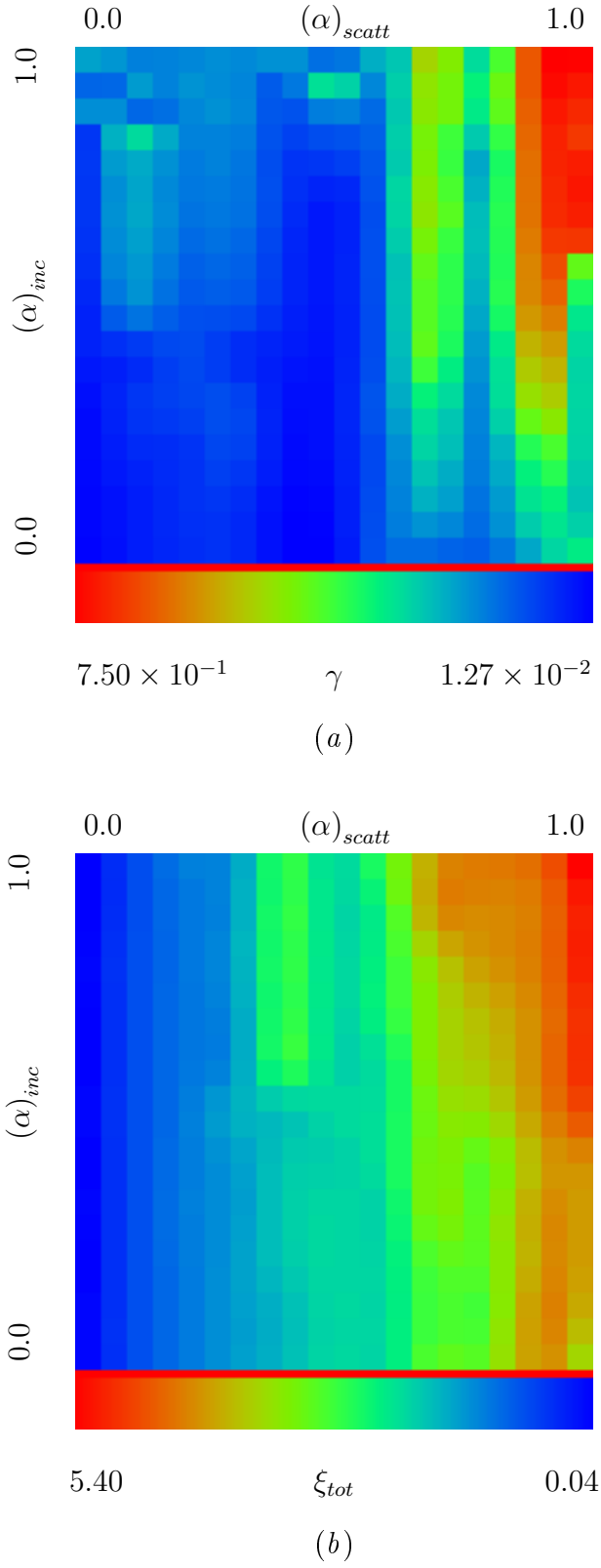

Fig. 6 - S. Caorsi *et al.*, "Analysis of the stability ..."

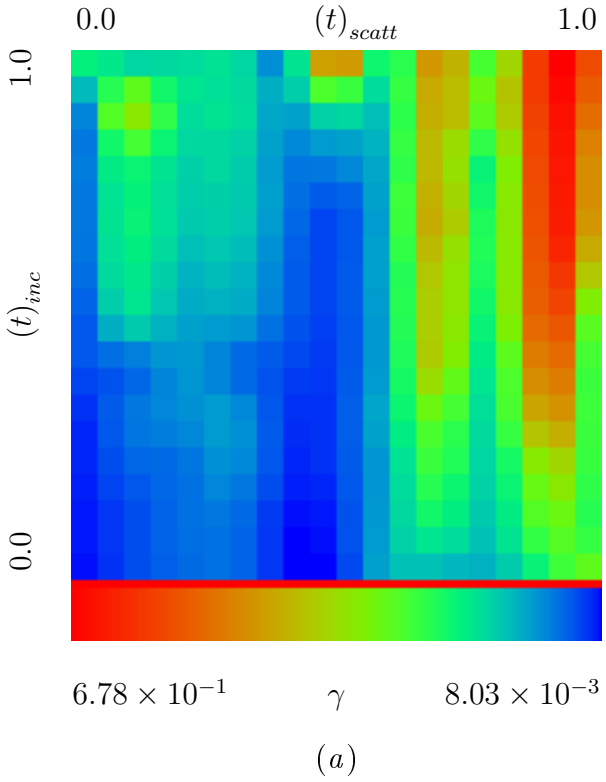

(a)

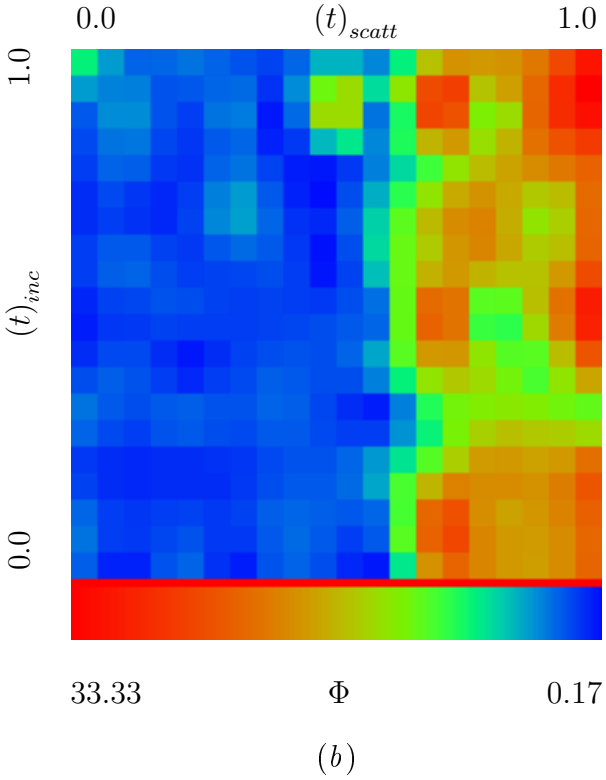

(b)

Fig. 7 (*I*) - S. Caorsi *et al.*, "Analysis of the stability ..."

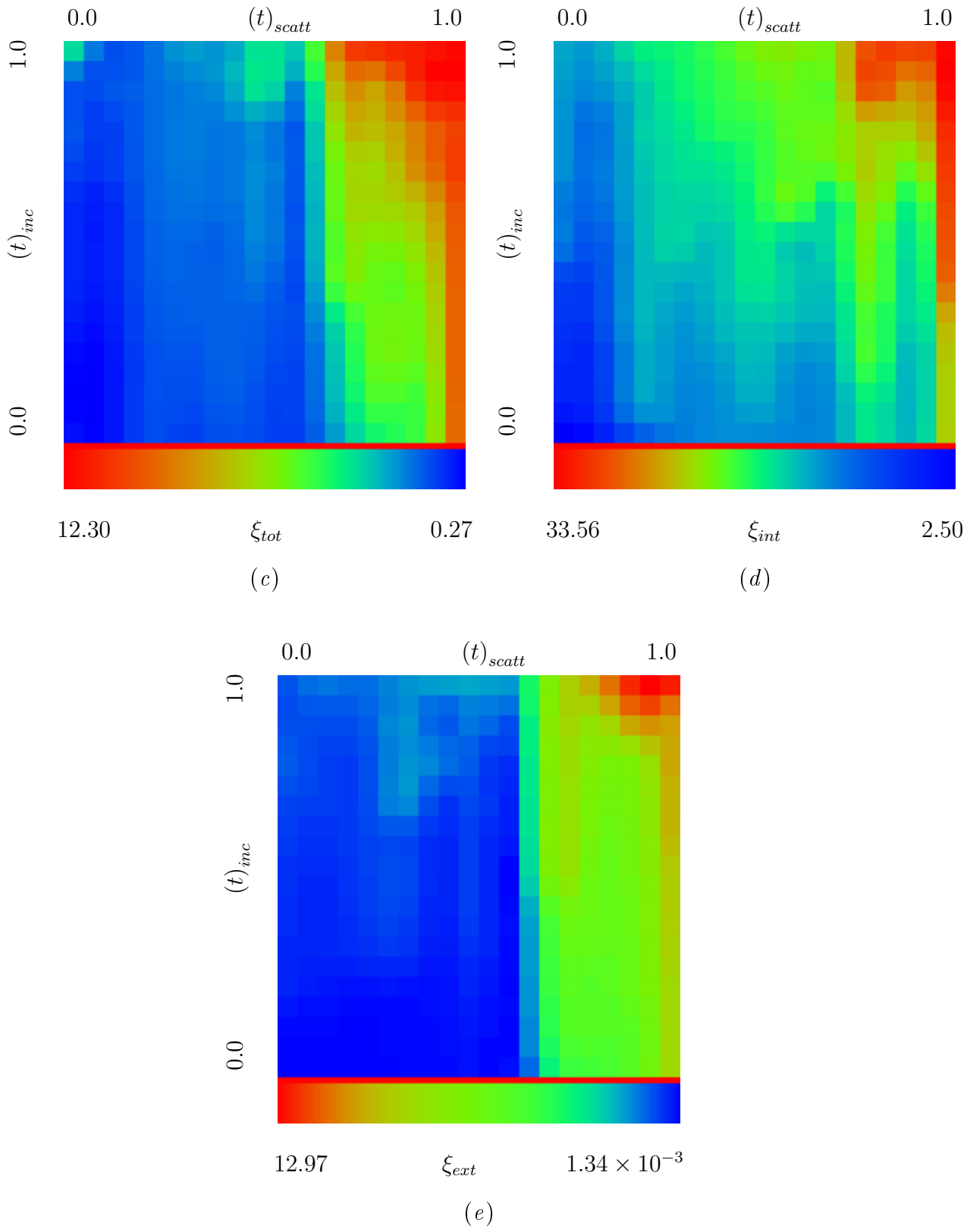

Fig. 7 (*II*) - S. Caorsi *et al.*, "Analysis of the stability ..."

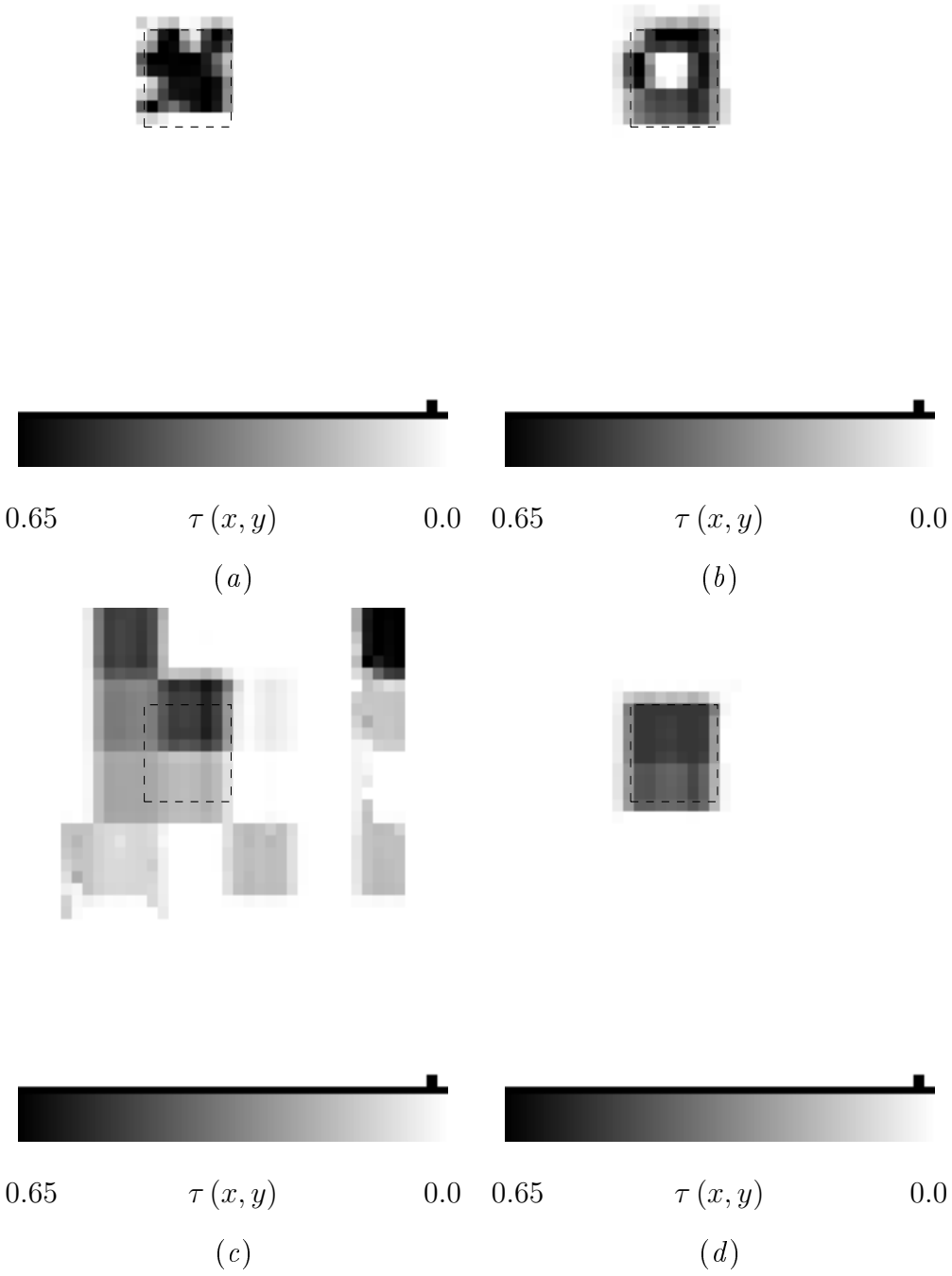

Fig. 8 (*I*) - S. Caorsi *et al.*, "Analysis of the stability ..."

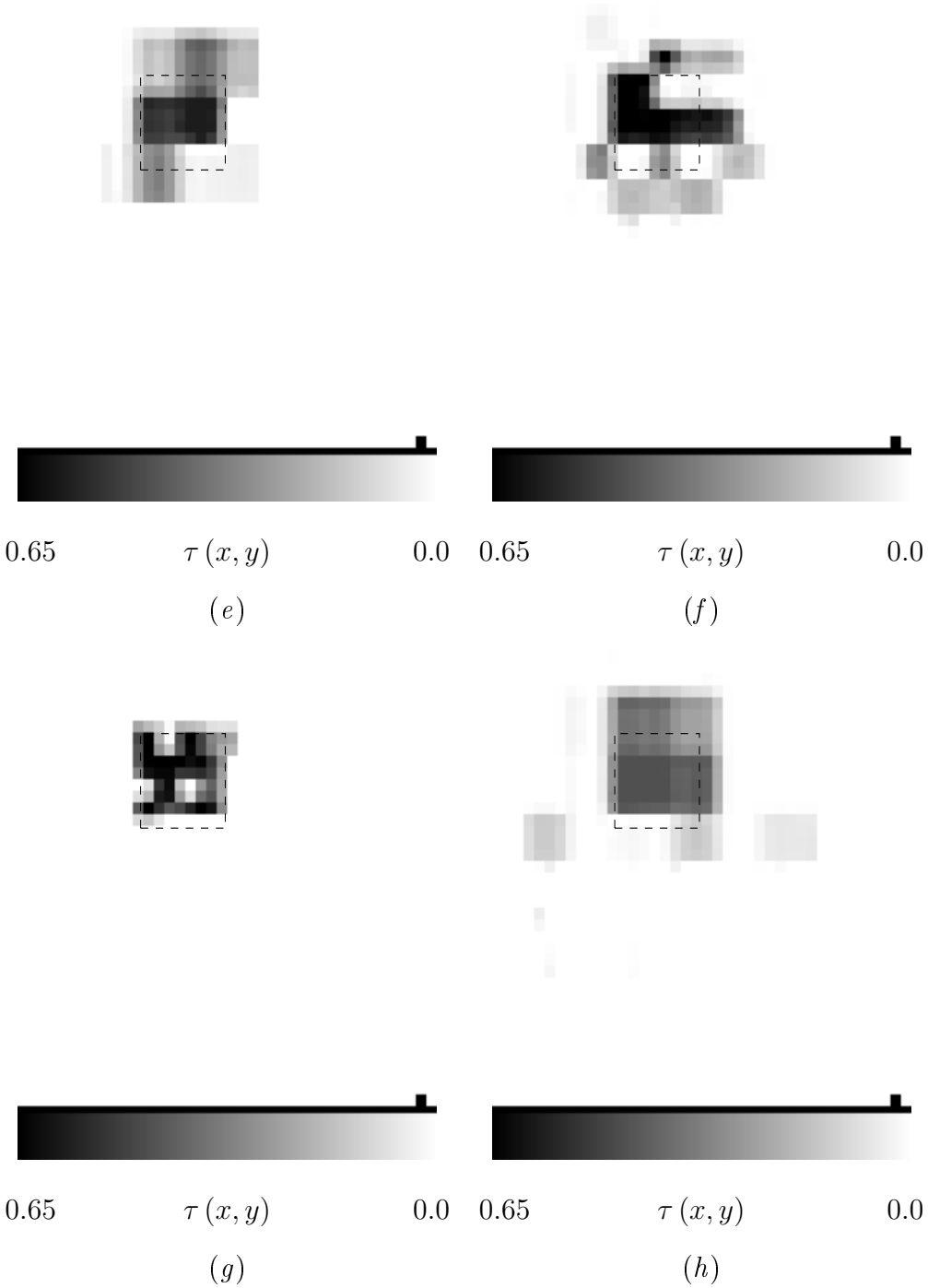

Fig. 8 (*II*) - S. Caorsi *et al.*, "Analysis of the stability ..."

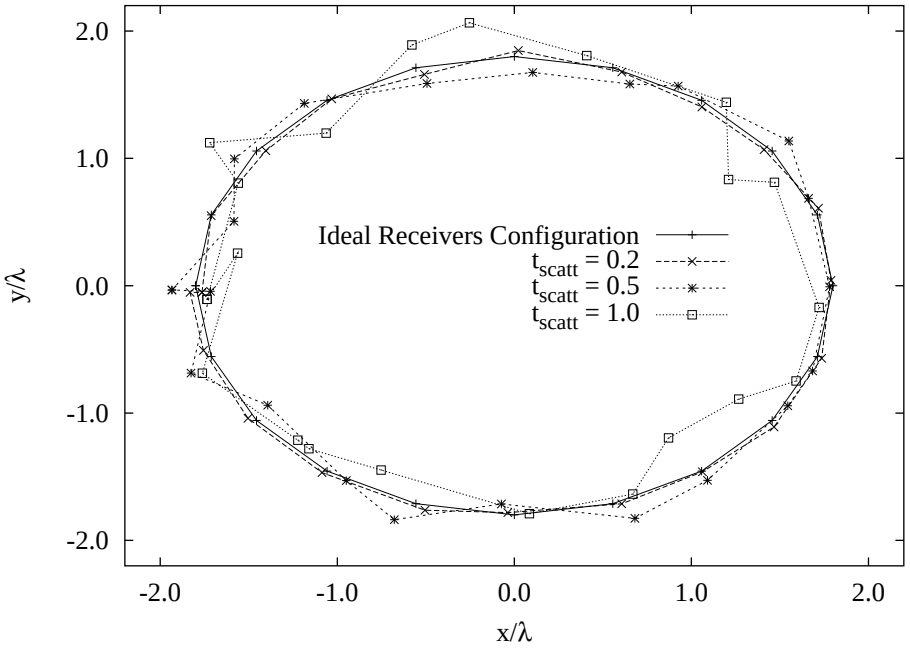

(a)

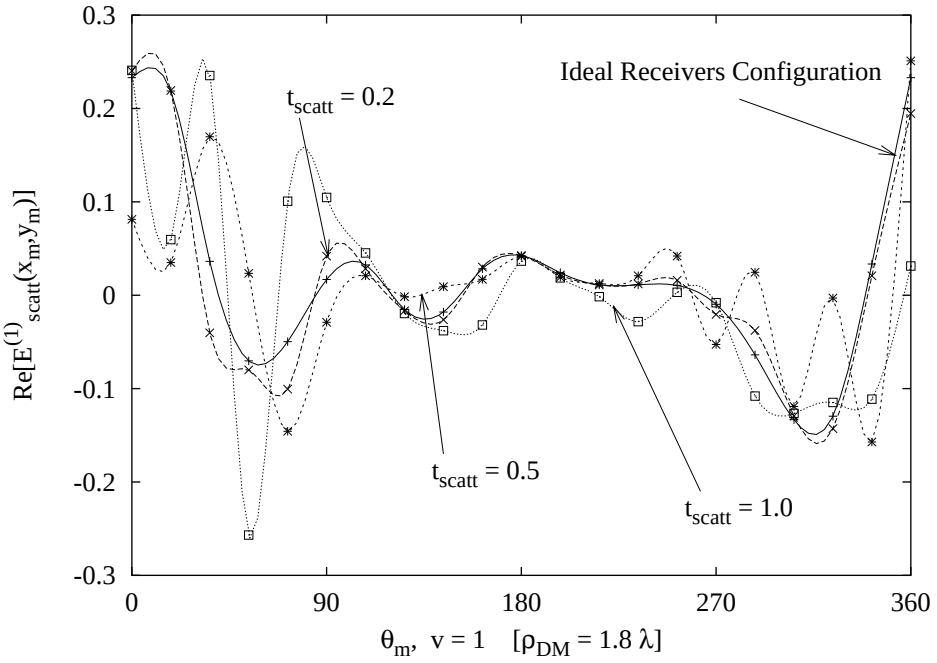

(b)

Fig. 9 (I) - S. Caorsi *et al.*, "Analysis of the stability ..."

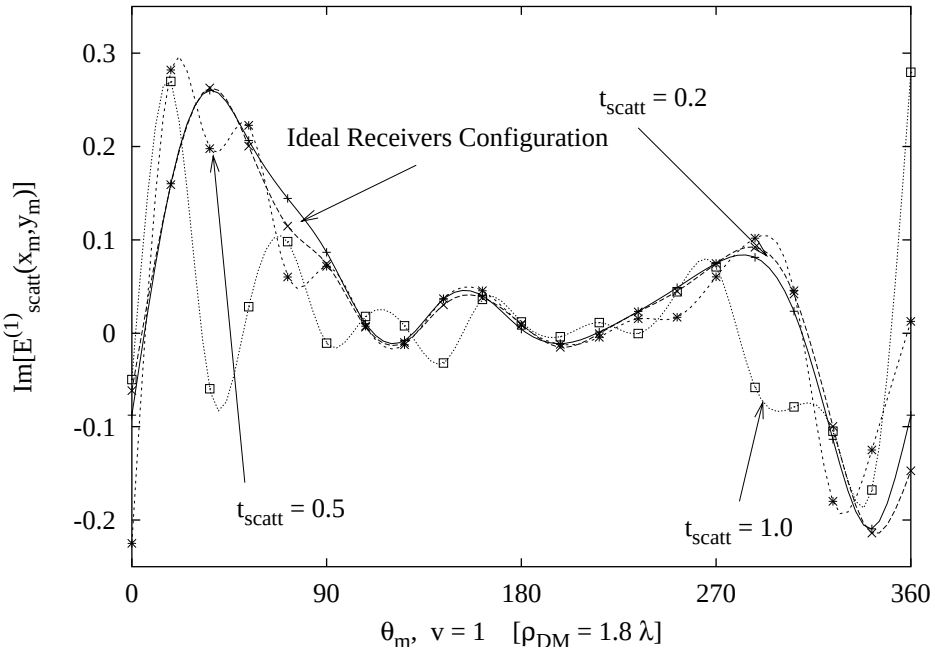

(c)

Fig. 9 (*II*) - S. Caorsi *et al.*, "Analysis of the stability ..."

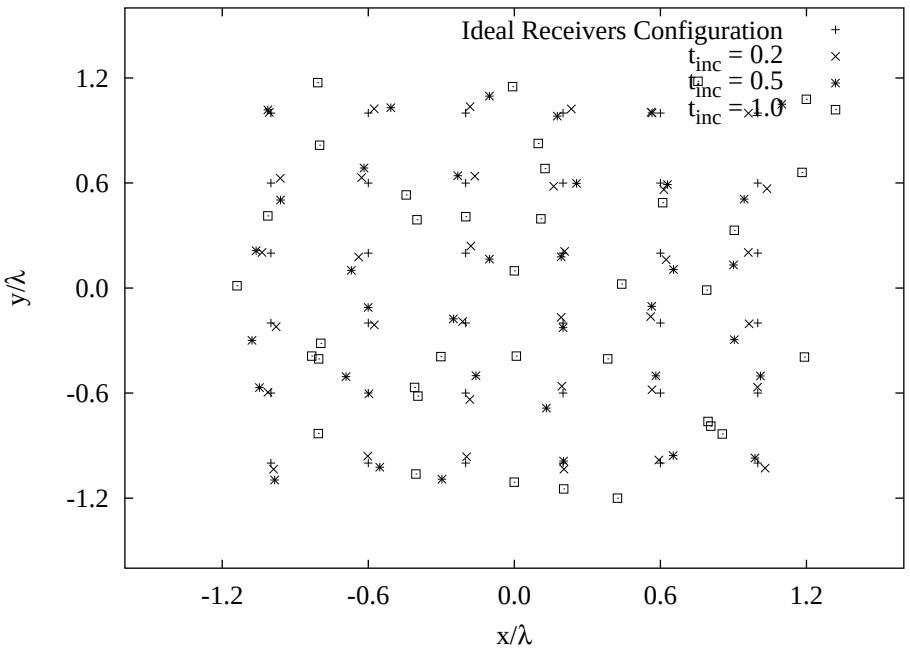

(a)

Fig. 10 (I) - S. Caorsi *et al.*, "Analysis of the stability ..."

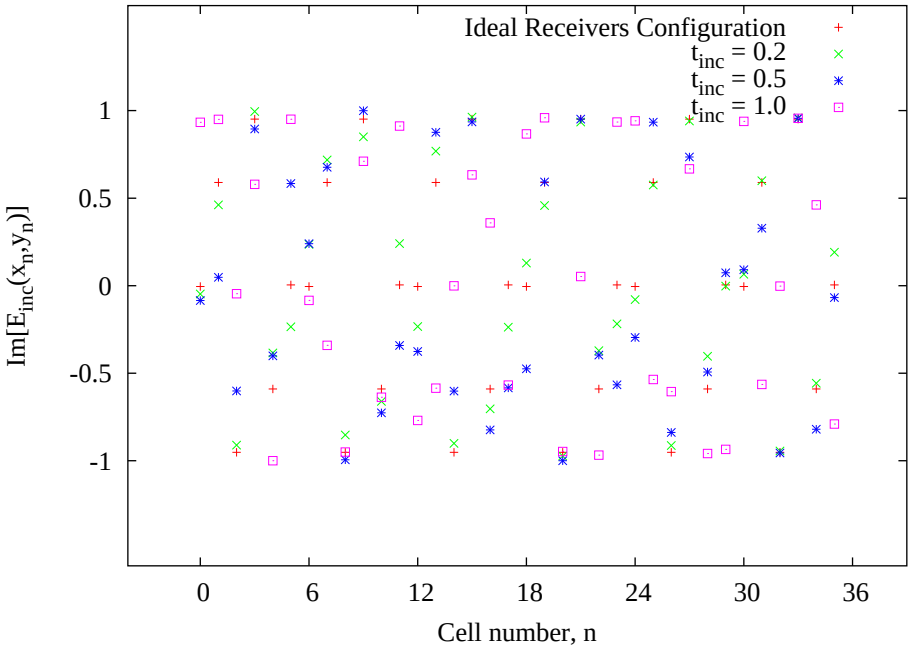

(b)

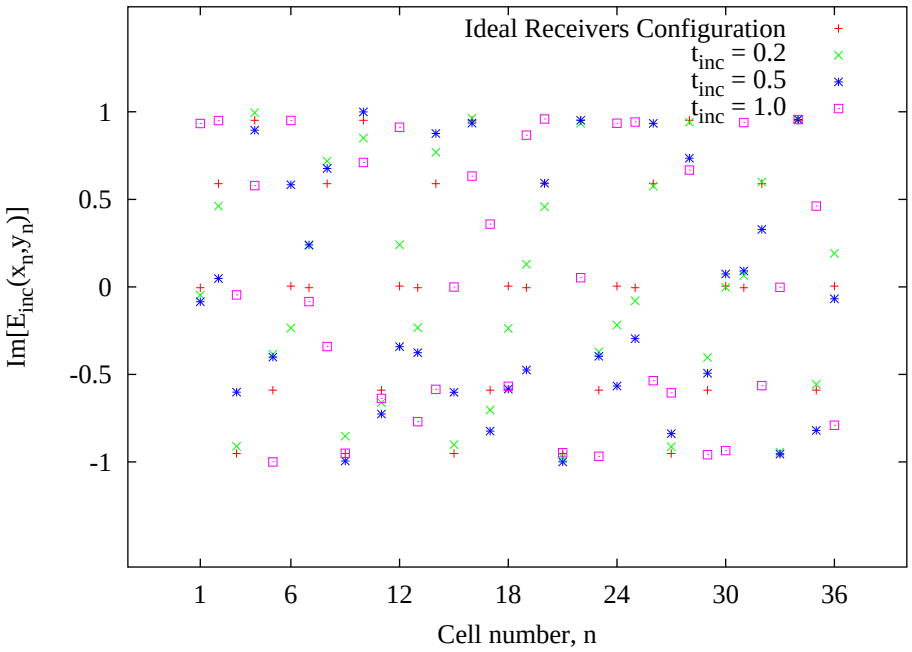

(c)

Fig. 10 (*II*) - S. Caorsi *et al.*, "Analysis of the stability ..."

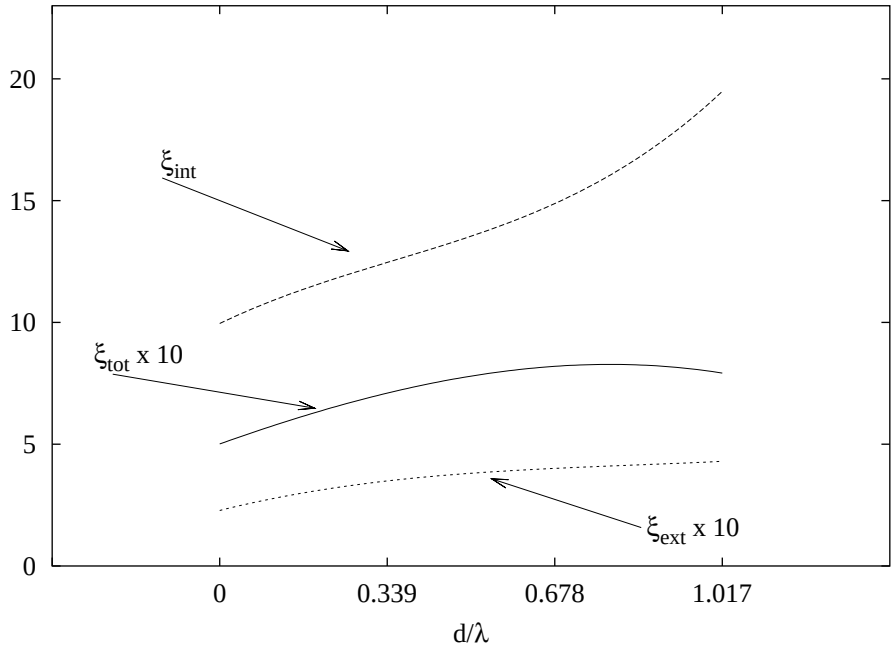

(*a*)

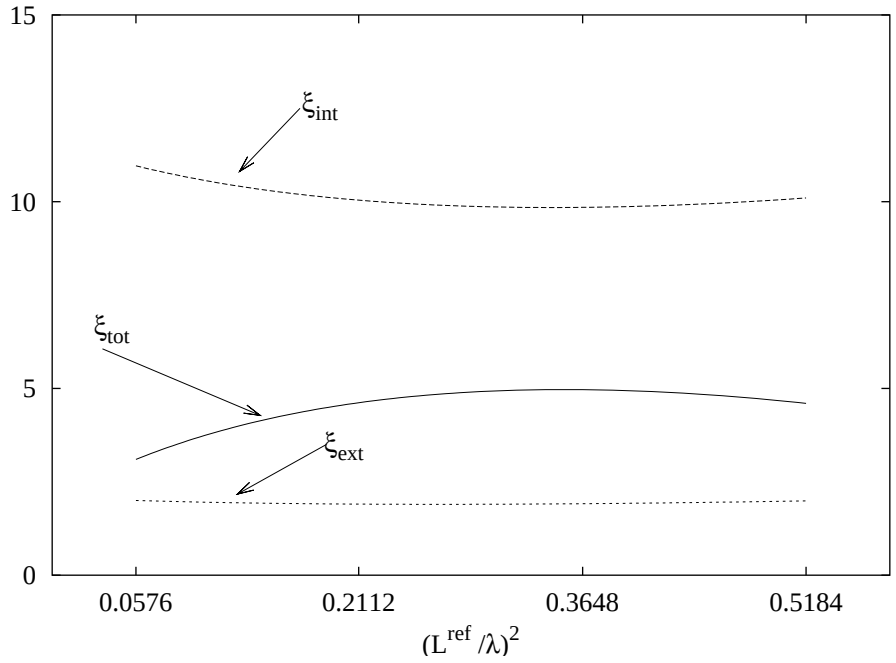

(*b*)

Fig. 11 (*I*) - S. Caorsi *et al.*, "Analysis of the stability ..."

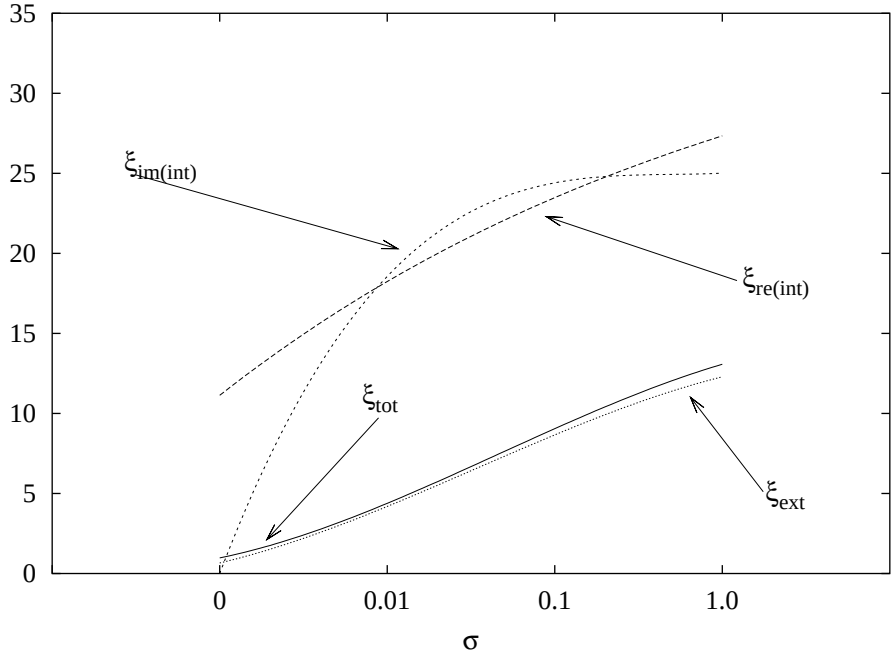

(c)

Fig. 11 (*II*) - S. Caorsi *et al.*, "Analysis of the stability ..."

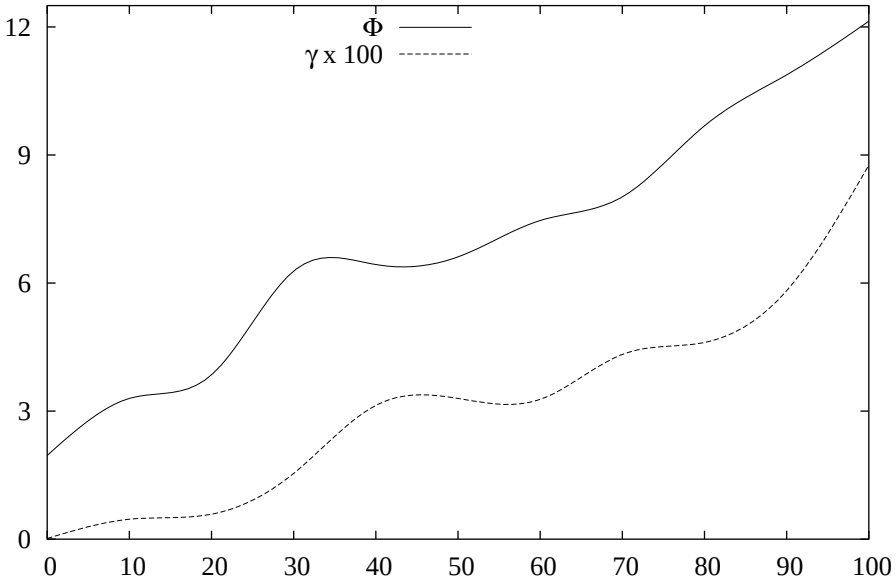

(a)

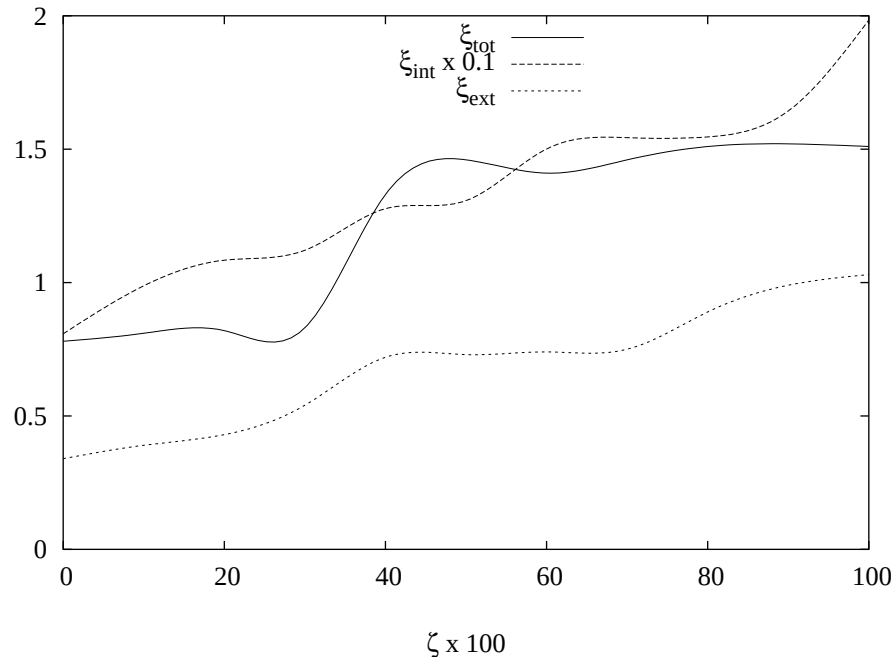

(b)

Fig. 12 - S. Caorsi *et al.*, "Analysis of the stability ..."

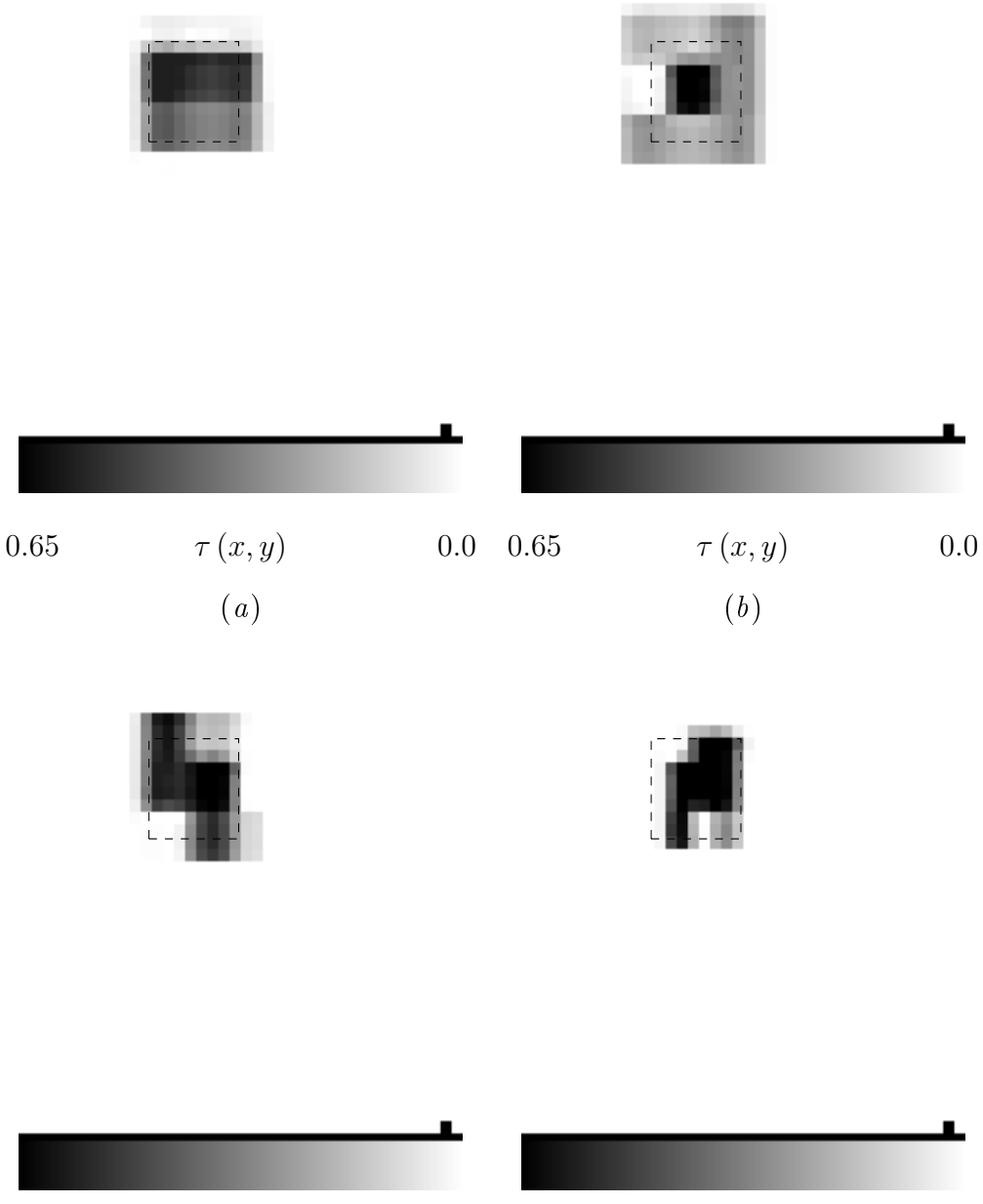

Fig. 13 - S. Caorsi *et al.*, "Analysis of the stability ..."

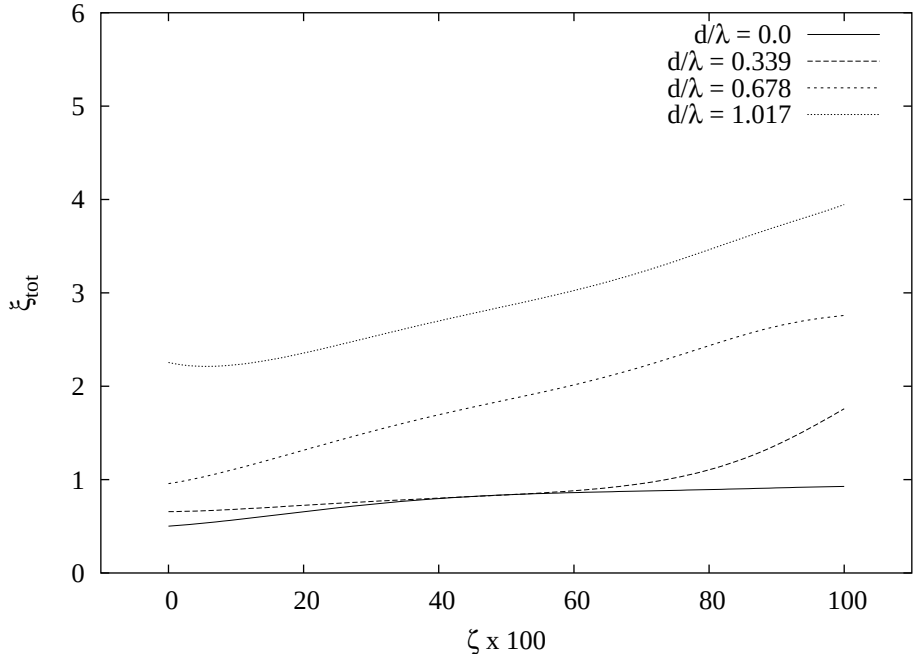

(a)

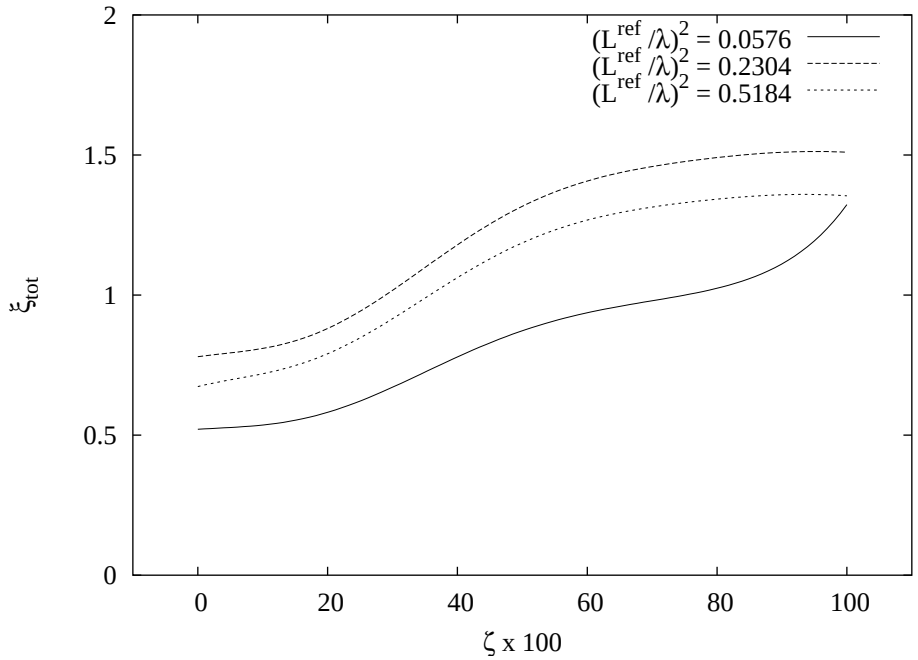

(b)

Fig. 14 (*I*) - S. Caorsi *et al.*, "Analysis of the stability ..."

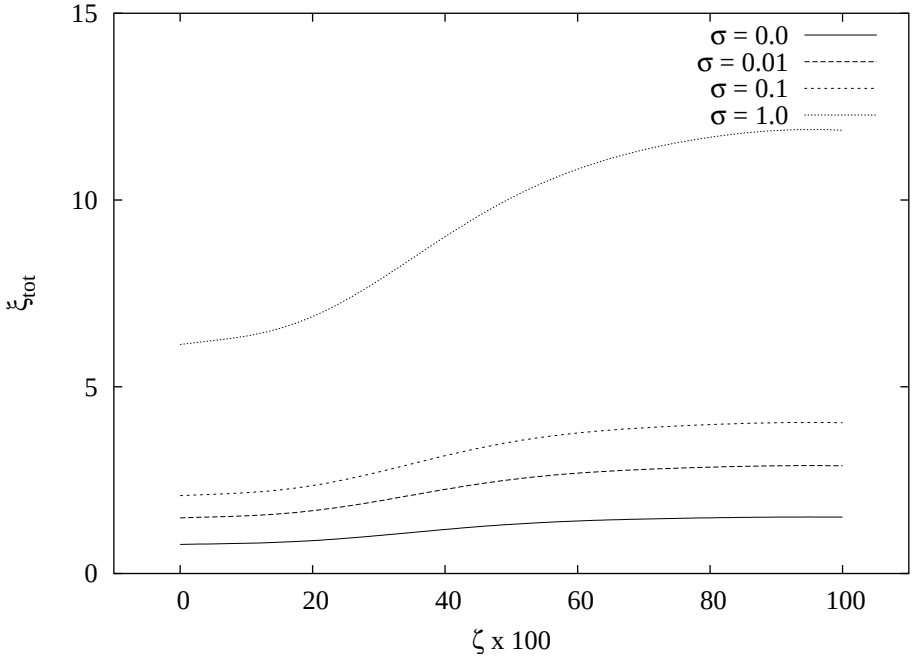

(c)

Fig. 14 (*II*) - S. Caorsi *et al.*, "Analysis of the stability ..."

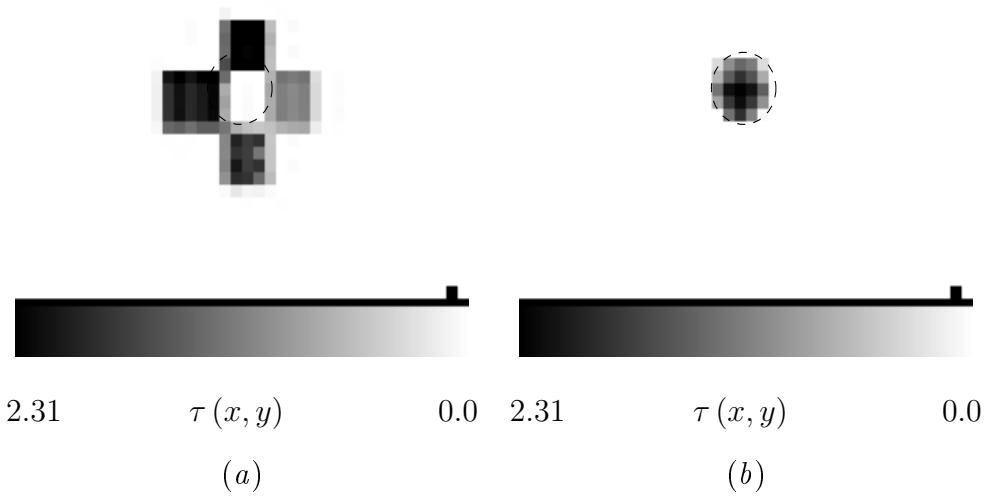

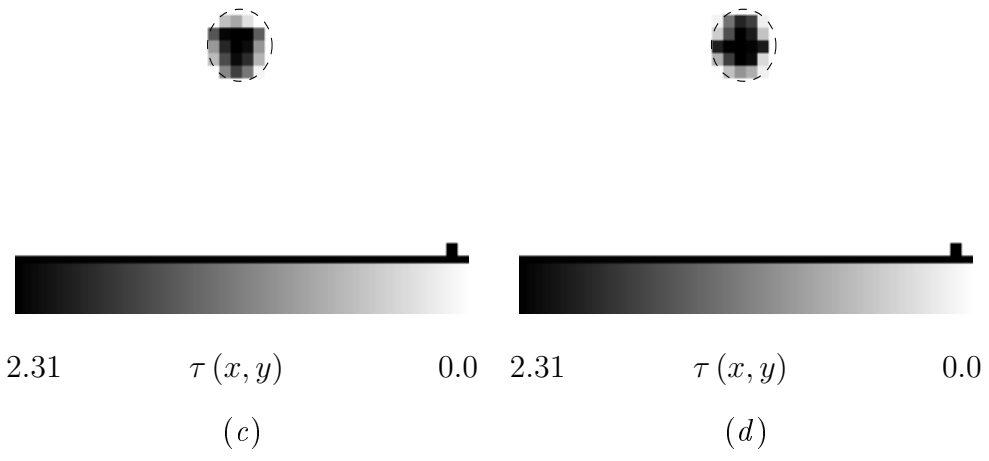

Fig. 15 (*I*) - S. Caorsi *et al.*, "Analysis of the stability ..."

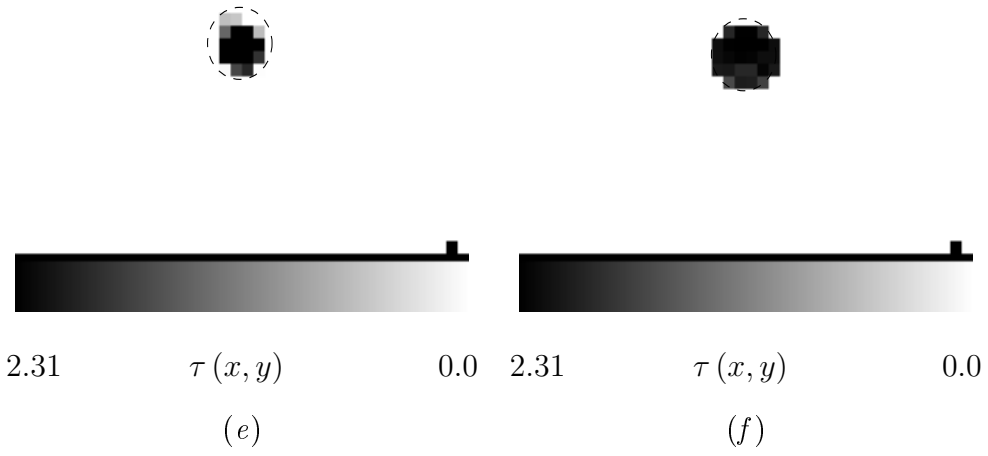

(e) (f)

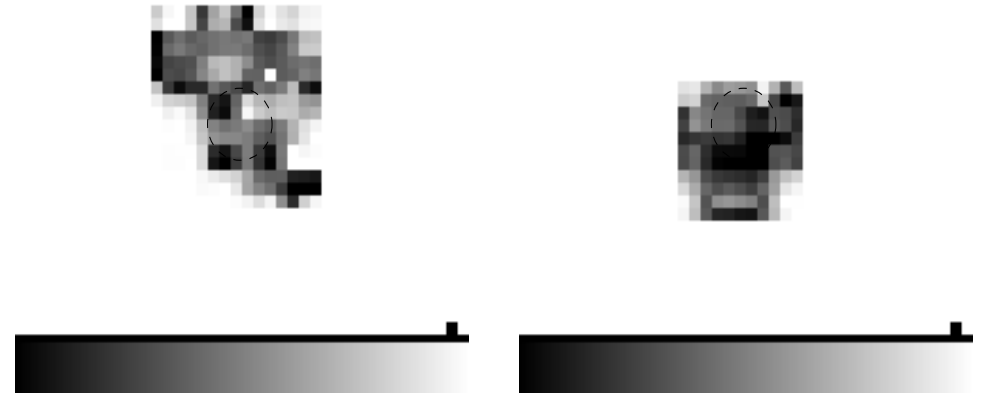

(g) (h)

Fig. 15 (*II*) - S. Caorsi *et al.*, "Analysis of the stability ..."

0.0 $Im\{\tau(x,y)\}$ 10.5

(a)

0.0 $Im\{\tau(x,y)\}$ 10.5

(b)

Fig. 16 - S. Caorsi *et al.*, "Analysis of the stability ..."

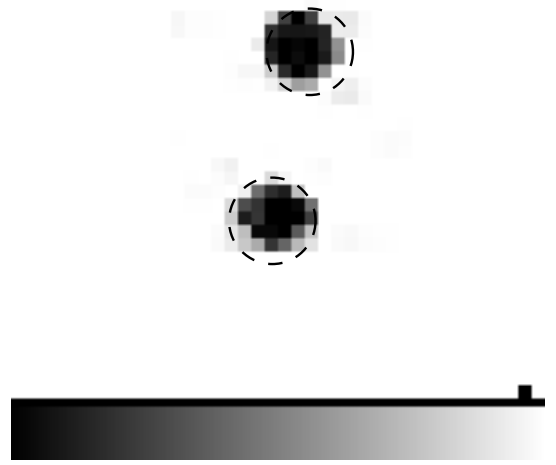

Fig. 17 - S. Caorsi *et al.*, "Analysis of the stability ..."

$(SNR)_{scatt}$	$(SNR)_{inc}$	γ	Φ	ξ_{tot}	ξ_{int}	ξ_{ext}
∞	∞	6.30×10^{-4}	0.20	0.11	6.64	3.0×10^{-8}
∞	20 dB	6.48×10^{-4}	10.03	0.88	10.81	0.67
∞	5 dB	2.12×10^{-2}	6.07	1.24	14.83	0.75
20 dB	∞	2.23×10^{-3}	11.89	0.86	8.42	0.64
5 dB	∞	1.48×10^{-2}	4.02	1.10	10.86	0.73
20 dB	20 dB	1.07×10^{-2}	12.92	0.97	11.13	0.66
5 dB	5 dB	5.50×10^{-2}	16.11	5.41	17.69	2.99

Tab. I - S. Caorsi *et al.*, "Analysis of the stability ..."

$(t)_{scatt}$	$(t)_{inc}$	γ	Φ	ξ_{tot}	ξ_{int}	ξ_{ext}
0.2	0.0	5.92×10^{-2}	8.02	1.35	9.94	0.25
0.5	0.0	1.82×10^{-2}	11.15	1.42	15.65	0.11
1.0	0.0	2.79×10^{-1}	31.34	9.50	23.46	8.92
0.0	0.2	1.99×10^{-2}	5.42	0.43	6.21	0.032
0.0	0.5	4.99×10^{-2}	8.39	0.89	11.44	0.55
0.0	1.0	1.58×10^{-2}	25.24	2.09	12.97	1.42
0.2	0.2	6.37×10^{-2}	8.45	1.39	13.71	0.17
0.5	0.5	3.77×10^{-2}	13.84	2.15	17.43	0.66
1.0	1.0	6.78×10^{-1}	33.33	12.30	33.56	12.97

Tab. II - S. Caorsi *et al.*, "Analysis of the stability ..."

	Min	Max	Av	Var
γ	1.62×10^{-4}	8.76×10^{-2}	3.25×10^{-2}	6.20×10^{-4}
Φ	1.95	12.13	6.96	9.07
ξ_{tot}	0.78	1.52	1.22	0.09
ξ_{int}	8.07	19.84	13.45	10.37
ξ_{ext}	0.34	1.02	0.68	0.05

Tab. III - S. Caorsi *et al.*, "Analysis of the stability ..."

f	$x_{c_{(S_{opt})}}$	$y_{c_{(S_{opt})}}$	$L_{(S_{opt})}$	$\tau^{(S_{opt})}(x,y)$		
				Min	Max	Av
1	−4.39	−31.01	84.72	0.32	0.69	0.58
2	−1.65	−26.00	33.38	1.06	2.17	1.98
3	−2.07	−26.79	32.98	1.07	2.20	1.97
4	−1.78	−26.15	30.72	1.47	2.15	1.99
5	−1.87	−25.90	28.58	1.33	2.31	1.98
6	−1.20	−33.20	32.76	1.50	2.10	2.02
7	−3.59	−14.23	97.06	0.56	2.28	1.68
8	−3.68	−38.46	76.46	0.32	2.30	1.77

Tab. IV - S. Caorsi *et al.*, "Analysis of the stability ..."